Physics – Uspekhi **63** (4) 342 – 364 (2020)

REVIEWS OF TOPICAL PROBLEMS PACS numbers: **61.46.–w**, 61.66.Fn, 61.82.Rx, 81.07.Wx

High-energy ball milling of nonstoichiometric compounds

A I Gusev

DOI: https://doi.org/10.3367/UFNe.2019.06.038581

Contents

Abstract. The preparation of nanocrystalline powders of nonstoichiometric compounds such as carbides and oxides by high-energy milling is considered. The modern state of milling models for nonstoichiometric compounds is described. The influence of nonstoichiometry on the particle size of the produced nanopowders is discussed. The model dependences of the size of nanopowder particles on the duration of milling and the composition of nonstoichiometric compounds are compared with the literature experimental results on the milling of nonstoichiometric carbides and oxides. Diffraction methods for the certification of nanopowders according to the size of the nanoparticles, the magnitude of microstrains, and the uniformity of the microstructure are considered in detail. The importance of taking into account the anisotropy of microstrains in milled nanopowders is shown.

Keywords: high-energy ball milling, nanopowders, nonstoichiometry, carbides, oxides, nanoparticle size, anisotropy of microstrains, X-ray and neutron diffraction

1. Introduction

Production of nanocrystalline substances and materials has been an extensively developing field of material science in the past decade due to the possibility of radically modifying the properties of solids in the nanocrystalline state [1–5]. For example, powders with different characteristics are needed to produce ceramics intended for different purposes. The size and shape as well as the specific surface area and chemical composition of particles are of paramount importance in the context of powder applications.

Disintegration of a solid under the effect of prolonged compressive, shearing, and bending strains leads to its gradual dispersion into a powder-like state. The powder particle size falls into the micrometer or nanometer range, depending on the energy applied. Mechanical fragmentation of powders proved a most efficient and productive method for producing various substances and materials in the nanocrystalline state; it is widely used in modern physical materials science [1–6].

Ball milling is a simple and efficient method for making nanocrystalline powders of various metals and alloys, oxides, carbides, sulfides, borides, and other compounds [1, 7–21] with particles up to 20 nm in size intended for superconducting ceramic materials, materials with magnetic anisotropy, superhard metal-cutting materials, nanocomposites, and superplastic ceramics. High-energy planetary, vibratory, whirlwind, and other mills, as well as attritors of different types, are used for grinding.

In the USSR, a large amount of research on the mechanical treatment of inorganic substances (with special reference to mechanochemistry) was performed based at the Institute of Solid State Chemistry and Processing of Mineral Raw Materials, Siberian Branch of the Russian Academy of Sciences (presently, Institute of Solid State Chemistry and Mechanochemistry, Siberian Branch of RAS) [6, 22].

The strength and the stress rupture of solids are the subjects of many original and generalizing studies focused on the description and analysis of the theory of strength and disintegration mechanisms (the interatomic bond breakage kinetics under elastic deformation, crack formation and growth, stress relaxation, etc.) (see, e.g., [6, 7, 23–27]). Some papers [6, 7, 28] present a qualitative description of milling and mechanochemical transformations using the term 'energo tension' to define the power consumed in a milling

A I Gusev. Institute of Solid State Chemistry,
Ural Branch of the Russian Academy of Sciences,
ul. Pervomaiskaya 91, 620990 Ekaterinburg, Russian Federation
Tel. (343) 362 35 23. Fax (343) 374 44 95. E-mail: gusev@ihim.uran.ru

Received 25 March 2019, revised 13 June 2019
Uspekhi Fizicheskikh Nauk **190** (4) 371 – 395 (2020)
Translated by Yu V Morozov; edited by V L Derbov

device per unit mass of the substance being treated. As to the ball milling of powders and its final result, i.e., the particle size, studies of this kind have until recently been performed at the empirical level due to a lack of models relating the size of particles in prepared nanocrystalline powders to the milling energy.

A few milling models were proposed in the late 20th–early 21th centuries [29–31]. According to [29], deformation during the mechanical abrasion of powders is localized in shear bands with high dislocation density. Dislocation model [30] is based on the assumption that any material (substance) is characterized by a certain minimal particle size $D_{\min}$ attainable by milling [32, 33]. According to [32, 33], size $D_{\min}$ is determined by equilibrium between the generation of a dislocation structure during milling and its relaxation upon reaching some stress level due to annihilation and recombination of dislocations into low-angle grain boundaries. Model [30] also takes into account the empirical data [32, 33] indicating that the size of metallic particles formed during milling under the identical conditions is inversely proportional to melting temperature T_m, shear G, and bulk K_c moduli. However, this model describes only experimental results and postulates the dependence of $D_{\min}$ on selected properties of materials (hardness, shear modulus, activation energy of vacancy migration) but does not establish the relationship between the milling energy or time and the post-milling particle size. The authors of [31] described, based on X-ray diffraction data, the size distribution of powder particles and estimated the degree of grinding but did not try to propose a predictive model. The dependence of particle size in nanocrystalline powders on milling characteristics was briefly considered for the first time in Ref. [34]. The milling model [34] was further developed in subsequent publications [35–37] with regard for the physical properties of a treated substance. Later authors [38, 39] improved the high-energy ball milling model [34–37] and elucidated the relationship between the particle size of the nanocrystalline powders obtained on the one hand and the milling energy, particle size, and mass of the initial powder, on the other hand.

Consideration of high-energy ball milling should be preceded by a brief discussion of the influence of the particle size on the physical properties of substances and materials. This issue has been addressed in detail in several reviews and monographs [1–5] with special reference to modification of the characteristics of solids associated with the diminishing size of their particles (crystallites).

The effect of particle size on the mechanical properties of metals, alloys, oxides, carbides, and other compounds has been most thoroughly investigated by testing microhardness H_V. A rise in H_V with decreasing particle size was documented in nanocrystalline Ag, Pd, Cu, Fe, Ni [40–44], Fe- and Ni-based alloys [45], and MgO [44]. Reducing grain size was also shown to lead to a significant (by a factor of 2–3) increase in the yield stress of nanocrystalline copper Cu and palladium Pd [40].

The importance of considering the powder granulometric composition is exemplified by the application of silicon carbide powder with a given particle size to ensure saturated vapor pressure for the sublimation growth of large SiC crystals [46]. According to [47], to increase the sublimation rate the initial SiC powder containing equal amounts of two fractions with 50- and 60–110-μm particles, respectively, should be used.

An example of the considerable improvement in powder properties by grain size manipulation is provided by hard WC−Co alloys, the properties of which are in many respects determined by the particle size of the initial tungsten carbide powder [48]. It was shown in [49] that the use of a WC nanopowder with a particle size of 50–60 nm allowed the optimal sintering temperature of a hard WC−Co alloy to be decreased by roughly 100 K and a denser alloy to be obtained. It was shown in [50, 51] that the use of WC nanopowders with a particle size of 35–40 nm allows obtaining WC−Co alloys having a denser fine-grained structure and enhanced hardness and fracture toughness than those of standard hard alloys.

The particle size influences the variation in the shape and boundaries of the phonon spectrum [5], as well as all the related properties, including heat capacity, thermal expansion, and Debye temperatures. It was shown in [52] that a decrease in the Ni powder particle size to 10–15 nm was accompanied by an increase in phonon state density in comparison with that in a coarse-grained powder. According to [53, 54], the heat capacity of Pb and Ag nanoparticles ~ 10 nm in size is 25–75% higher than these metals have in a coarse-grained state. A 15–25% rise in the thermal expansion coefficient of nanocrystalline lead sulfide compared with that in coarse-crystalline PbS is reported in [55–59]. The increased heat capacity and thermal expansion coefficient with a simultaneous decrease in the bulk modulus in nanocrystalline silver sulfide in comparison with the same characteristics of coarse-grained Ag_2S were demonstrated in Refs [58–66].

One-dimensional ZnS nanowires and their arrays are characterized by enhanced emission properties compared with coarse-crystalline zinc sulfide [67, 68].

In other words, the size of particles (grains, crystallites) exerts a considerable influence on the properties of substances and materials. That is why it is so important to produce substances and materials with controllable predetermined particle size. High-energy ball milling provides an efficient tool for this purpose.

2. Milling model

Let us consider in brief a model of mechanical powder milling to a smaller particle size [34–39] and its applicability to estimating the powder particle size as a function of the milling energy E_{mill}, mass M of the initial powder and particle size D_{in} of the initial powder.

The particle volume and surface area in an initial powder are equal to $V_{\text{in}} = f_v D_{\text{in}}^3$ and $S_{\text{in}} = f_s D_{\text{in}}^2$, respectively, where f_v and f_s are the form factors of the volume and surface area (i.e., coefficients of proportionality depending on the solid body shape). For spherical particles with diameter D_{in}, the form factors are $f_v = \pi/6$ and $f_s = \pi$, whence $f_s/f_v = 6$. For cubic particles with edge length D_{in}, the form factors $f_v = 1$ and $f_s = 6$; therefore, $f_s/f_v = 6$, too. For particles shaped like thin plates, $f_s/f_v \approx 2$. If, in the first approximation, the particles of the initial and ball milled powders have the same shape (or the particle shape distribution in the initial and ball milled powders is the same), the ratio of the volume and surface area form factors f_s/f_v is constant.

Let an initial powder have density d_d and mass M. Then, the number of particles in the initial powder is $M/d_d V_{\text{in}} = M/(d_d f_v D_{\text{in}}^3)$. According to [25], the energy is consumed during powder milling to rupture interatomic bonds in the crystal and form an additional surface upon cleaving the crystal particles. Therefore, the milling energy E_{mill} can be

written in the form

$$E_{\text{mill}} = \frac{M}{d_{\text{d}} f_{\text{v}} D_{\text{in}}^3} (E_{\text{rupt}} + E_{\text{surf}}) , \tag{1}$$

where E_{rupt} is the energy consumed to break intreratomic bonds in a single particle of the initial powder, E_{surf} is the energy consumed to form the additional surface upon cleaving one particle of the initial powder.

Crushing a single particle of the initial powder produces n smaller particles with average linear dimension D; the volume and the surface area are $f_{\text{v}} D^3$ and $f_{\text{s}} D^2$, respectively. Since $V_{\text{in}} = n f_{\text{v}} D^3$, then $n = D_{\text{in}}^3 / D^3$. In this case, the surface area of all the particles formed by grinding equals $S = n f_{\text{s}} D^2 = f_{\text{s}} D_{\text{in}}^3 / D$ and the surface area increment is

$$\Delta S = S - S_{\text{in}} = \frac{f_{\text{s}} D_{\text{in}}^2 (D_{\text{in}} - D)}{D} . \tag{2}$$

A crystal cleavage occurs along slip planes. Let the slip plane area per unit cell of a crystal be s_{f}; then, the number of planes along which cleavage proceeds is $\Delta S / s_{\text{f}}$. If q interatomic bonds with energy u pass through every slip plane per unit cell, the energy consumed for the rupture of bonds during grinding of one particle of the initial powder is

$$E_{\text{rupt}} = \frac{q u f_{\text{s}} D_{\text{in}}^2 (D_{\text{in}} - D)}{s_{\text{f}} D} . \tag{3}$$

The increment of the surface energy related to an increase in the particle surface area by ΔS is $\Delta E_{\text{s}} = \gamma \Delta S$, where γ is the specific (per unit interface area) excess energy generated by the disordered network of edge dislocations. According to [69], the energy E_{surf} consumed to create the additional surface upon cleavage of crystalline particles is hundreds of times higher than the surface energy increment ΔE_{s}, i.e., $E_{\text{surf}} = \beta \Delta E_{\text{s}} = \beta \gamma \Delta S$, where β is the proportionality coefficient. Therefore,

$$E_{\text{surf}} = \beta \gamma \Delta S = \frac{\beta \gamma f_{\text{s}} D_{\text{in}}^2 (D_{\text{in}} - D)}{D} . \tag{4}$$

In ball milling, as in other mechanical deformation techniques, the grain or particle boundaries (i.e., interfaces) are nonequilibrium. The authors of [70] proposed a nonequilibrium grain boundary model taking account of chaotic arrays of introduced grain boundary dislocations. It allowed deriving the expression for the root mean square elastic strain and estimating the excess energy of interfaces directly related to the appearance of elastic stress fields. For example, an expression was obtained for the specific interfacial excess energy γ generated by the chaotic network of edge dislocations with the Burgers vector $\mathbf{b} = (\pm b, 0, 0)$:

$$\gamma = \frac{G b^2 \rho \ln (D_{\text{in}}/2b)}{4\pi (1 - \nu)} . \tag{5}$$

Quantities G and ν in (5) are the shear modulus and the Poisson coefficient of the substance, $b = |\mathbf{b}|$ is the Burgers vector modulus, and $\rho \approx \rho_{\text{V}} D/3$ and ρ_{V} are linear and bulk dislocation densities, respectively.

In accordance with [71], the bulk density of dislocations chaotically distributed in the grain body equals the geometric mean of dislocations density $\rho_{\text{D}} = 3/D^2$, related to the grain size D, and dislocation density $\rho_{\text{s}} = C\varepsilon^2/b^2$, related to microstrains ε, i.e.,

$$\rho_{\text{V}} = (\rho_{\text{D}} \rho_{\text{s}})^{1/2} . \tag{6}$$

Taking into account (6), the linear density of dislocations ρ equals

$$\rho \approx \frac{\rho_{\text{V}} D}{3} = \sqrt{\frac{3}{D^2} \frac{C\varepsilon^2}{b^2}} \frac{D}{3} = \sqrt{3C} \frac{\varepsilon}{3b} , \tag{7}$$

where C is constant for a given substance assuming a value from 2 to 25 [71].

Writing the specific excess energy γ (5) with regard for (7) and substituting it into (4) we find yield energy E_{surf} consumed to create an additional surface upon cleaving a crystalline particle [34–37]:

$$E_{\text{surf}} = \frac{\beta \gamma f_{\text{s}} D_{\text{in}}^2 (D_{\text{in}} - D)}{D} = \frac{\sqrt{3C} \beta f_{\text{s}}}{12\pi} \frac{G b D_{\text{in}}^2 (D_{\text{in}} - D) \ln (D_{\text{in}}/2b)}{1 - \nu} \frac{\varepsilon}{D} . \tag{8}$$

Substituting (3) and (8) into (1) yields the formula relating the milling energy E_{mill} to the mean size of particles D produced by grinding:

$$E_{\text{mill}} = \frac{M f_{\text{s}}}{d_{\text{d}} f_{\text{v}}} \frac{D_{\text{in}} - D}{D D_{\text{in}}} \frac{12\pi (1 - \nu) q u + \sqrt{3C} \beta G b s_{\text{f}} \varepsilon \ln (D_{\text{in}}/2b)}{12\pi (1 - \nu) s_{\text{f}}} . \tag{9}$$

It follows from (9) that milling introduces microdeformations into resulting particles, besides reducing their mean size.

For a concrete substance, d_{d}, f_{s}, f_{v}, q, u, C, β, G, ν, b, s_{f} values are fixed, the energy of milling is proportional to its duration t, and the particle size and microstrains are functions of milling time t and powder mass M. Therefore, expression (9) was transformed in [38, 39] into

$$E_{\text{mill}}(t) = \frac{M \left[D_{\text{in}} - D(t, M) \right] \left[A + B\varepsilon(t, M) \ln (D_{\text{in}}/2b) \right]}{D(t, M) D_{\text{in}}} , \tag{10}$$

whence

$$D(t, M) = \frac{M \left[A + B\varepsilon(t, M) \ln (D_{\text{in}}/2b) \right]}{E_{\text{mill}}(t) + M \left[A + B\varepsilon(t, M) \ln (D_{\text{in}}/2b) \right] / D_{\text{in}}} , \tag{11}$$

where

$$A = \frac{f_{\text{s}}}{f_{\text{v}}} \frac{q u}{s_{\text{f}} d_{\text{d}}} , \qquad B = \frac{f_{\text{s}}}{f_{\text{v}}} \frac{\beta G b \sqrt{3C}}{12\pi (1 - \nu) d_{\text{d}}}$$

are certain constants characteristic of a given substance. Obviously, formula (11) satisfies the edge condition $D(0, M) = D_{\text{in}}$, since the milling energy $E_{\text{mill}}(0) = 0$ and microstrains $\varepsilon(0, M) = 0$ at the initial time point $t = 0$. It follows from (11) that the appearance of microstrains ε slows down powder fragmentation. Formula (11) is the basic expression in the milling model defining the mean particle size as a function of the applied milling energy $E_{\text{mill}}(t) \sim kt$. The milling time t is the most important parameter. Usually, time t is chosen so as to enable the achievement of a stable equilibrium between destruction and cold welding of the powder particle. The time needed for the purpose varies depending of the mill type, the ratio of the ball mass to the

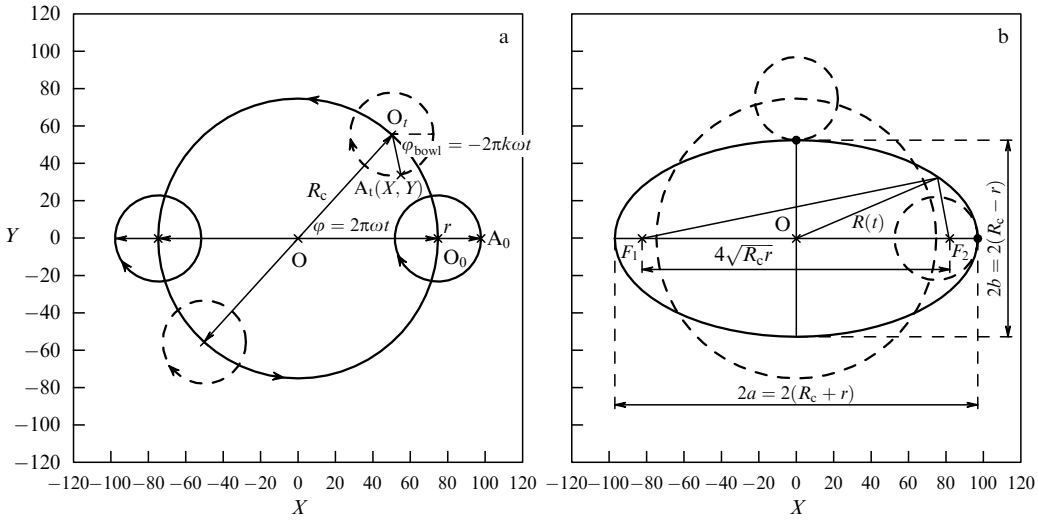

Figure 1. (a) The motion of a bearing disk and grinding bowl in a Retsch PM-200 mill and (b) the elliptic trajectory of the motion of milling balls at $k = 1$ [36]. $R_c = 0.075$ m is the radius of the circle along which the grinding bowl axis moves, $r = 0.0225$ m is the internal radius of the bowl, ω is the angular velocity of rotation of the bearing disk, k is the ratio of the bowl angular velocity to the bearing disk angular velocity, $\varphi = 2\pi\omega t$ and $\varphi_{bowl} = -2\pi k\omega t$ are the angles through which the bearing disk and the grinding bowl rotate over time t, respectively, and F_1 and F_2 are the foci of the elliptic trajectory.

powder mass, and the milling temperature. Coefficient k in the milling energy $E_{mill}(t)$ assumes different forms, depending on the design of the milling machine (high-energy planetary, ball, or vibratory) and the mechanics of the milling body movement.

Initial particle size D_{in} and fixed milling time t being known, the dependence of particle size D of the milled powder on mass M (load) of the initial substance is described by the function

$$D(t = \text{const}, M) = \frac{D_{in} M}{K D_{in} + M}\,, \tag{12}$$

where

$$K = \frac{E(t = \text{const})}{A + B\left[\ln\left(D_{in}/2b\right)\right]\varepsilon(t = \text{const}, M)}$$

is constant for a given time t. In other words, the smaller the mass of the loaded substance at the same milling time, the smaller the particle size in the powder produced.

The value of microstrains $\varepsilon = \Delta l/l \equiv \Delta d/d$ characterizes the uniform deformation averaged over the crystal volume, i.e., the relative change Δd in interplanar spacing d compared to its change in a perfect crystal. According to the Hooke law in the general case, $\Delta l/l = \sigma/E$. The fracture begins when a critical value of stress, σ_{max}, equal to the strength of the substance at a given deformation type, is attained; therefore, $\varepsilon_{max} = \sigma_{max}/E$, where E is the respective elasticity modulus. Microstrains ε vary from zero at $t = 0$ to some limiting value ε_{max} above which the crystal lattice of the ball-milled substance is destroyed. When milling time t is constant, the value of microstrains decreases with the growth of the mass of the ball-milled substance. With this in mind, in [39] the dependence of microstrains ε on milling time t and mass M of a given substance was proposed to be described by the empirical function

$$\varepsilon(t, M) = \varepsilon_{max}\frac{t}{t+\tau}\frac{M}{M+p} \equiv \frac{\sigma_{max}}{E}\frac{t}{t+\tau}\frac{M}{M+p}\,,$$

where τ and p are the normalizing parameters.

To obtain nanocrystalline powders of different substances and compounds for the purpose of research, planetary ball mills are most frequently used.

The milling energy E_{mill} depends on the design specs of the mill and movement of the milling bodies in the milling chamber; it is also a function of milling time t. The theoretical time dependence of the milling energy E_{mill} was elucidated in Ref. [36] by an example of using a PM-200 Retsch planetary ball mill. It was shown (see (11)) that the energy $E_{mill}(t)$ consumed to mill a powder is a basic parameter of the model [34–39]. It is easy to demonstrate that the expression derived in [36] for the milling energy $E_{mill}(t)$ can be used to describe milling in RITSCH Pulverisette planetary ball mills.

2.1 Mechanics of grinding ball motion

PM-200 Retsch and RITSCH Pulverisette-7 Premium line planetary ball mills each contain two grinding bowls with a volume of 50 or 45 ml, respectively, positioned symmetric with respect to each other at the periphery of the bearing disk. Materials of different hardness (from soft to extremely hard) are milled in steel grinding bowls with a layer of agate SiO_2, sintered corundum Al_2O_3, silicon nitride Si_3N_4, or zirconium oxide ZrO_2 lining the inner wall. Superhard materials like carbides are milled in bowls intended for work in extreme conditions (long-term grinding at a maximum rotational speed and mechanical stress) and having the inner wall coated with a hard WC−6 weight % Co alloy with a cobalt binder. In this case, grinding balls 3 mm in diameter from the same alloy are used.

Directions of rotation of bearing disk and grinding bowls in the PM-200 Retsch and RITSCH Pulverisette-7 are similar, with the disks rotating in one direction and the bowls in the opposite one. To analytically estimate the energy $E_{mill}(t)$ consumed to grind a powder in the mills, the authors of [36] introduced in the general form basic equations of motion describing ball movements in the grinding bowls. A schematic of bearing disk and grinding bowl motion is presented in Fig. 1a. The powder and milling balls in the rotating bowl are subjected to the action of centrifugal force; therefore, the balls

come into contact with powder particles at the inner wall of the bowl.

Let R_c be the radius of the circle described by the bowl axis, r the internal radius of the bowl, ω the angular rotation speed of the bearing disk, $\varphi = 2\pi\omega t$ the angle of bearing disk rotation for time t, $\omega_c = -k\omega$ the angular velocity of rotation of the bowl, and k the coefficient characterizing the difference between the angular rotation velocities of the disk and the bowl. Because the milling balls in the rotating bowl experience the action of centrifugal force, each ball is in contact with the inner wall of the bowl. Assume that a certain ball happens to be at point A_0 inside the bowl at the initial moment of time $t_0 = 0$. Then, the position of the bowl axis O_t at an arbitrary time point t is determined by the coordinates

$$\left.\begin{aligned} x_0 &= R_c \cos(2\pi\omega t) \\ y_0 &= R_c \sin(2\pi\omega t) \end{aligned}\right\}. \tag{13}$$

For the same time t, the ball coordinates with respect to the bowl rotation axis will change as a result of bowl rotation in the opposite direction with the angular speed $-k\omega$ and become

$$\left.\begin{aligned} x &= r\cos(-2\pi k\omega t) = r\cos(2\pi k\omega t) \\ y &= r\sin(-2\pi k\omega t) = -r\sin(2\pi k\omega t) \end{aligned}\right\}. \tag{14}$$

It can be supposed taking into account (13) and (14) that the ball initially located at the position A_0 after time t will be in the position A_t with coordinates

$$\left.\begin{aligned} X &= x_0 + x = R_c\cos(2\pi\omega t) + r\cos(2\pi k\omega t) \\ Y &= y_0 + y = R_c\sin(2\pi\omega t) - r\sin(2\pi k\omega t) \end{aligned}\right\}. \tag{15}$$

The distance between the center of the trajectory (the disk rotation center) and its arbitrary point at which a ball happened to be at time t is

$$\begin{aligned} R(t) &= \left[X^2 + Y^2\right]^{1/2} \\ &= \left\{R_c^2 + r^2 + 2R_c r\cos\left[2\pi(k+1)\omega t\right]\right\}^{1/2}. \end{aligned} \tag{16}$$

At the initial instant of mill rotation, the balls are in contact with the bowl inner wall and displaced with respect to a given ball through an arbitrary angle α. Clearly, the motion trajectory of a ball whose position is displaced by angle α with respect to that of the former ball will be turned at the same angle α relative the trajectory of the first ball. The coordinates of this ball can be represented as

$$\left.\begin{aligned} X &= R_c\cos(2\pi\omega t) + r\cos(2\pi k\omega t - \alpha) \\ Y &= R_c\sin(2\pi\omega t) - r\sin(2\pi k\omega t - \alpha) \end{aligned}\right\}. \tag{17}$$

As a result, the collective motion of all balls in the approximation of their independent movements is a set of the same-type trajectories turned with respect to each other.

The design of the PM-200 Retsch and RITSCH Pulverisette-7 mills ensures angular rotation rates of the disk and the bowl of the same absolute value, i.e., coefficient $k = 1$. At $k = 1$, the motion trajectory of a milling ball is an ellipse (Fig. 1b) with axes $2(R_c + r)$ and $2(R_c - r)$ described in a parametric form as $X = (R_c + r)\cos(2\pi\omega t)$, $Y = (R_c - r)\sin(2\pi\omega t)$. The instantaneous radius of the ball's elliptical path is $R(t) \equiv R(\varphi)$, i.e., the distance between any of its points and the center equals

$$\begin{aligned} R(t) &= \left[X^2 + Y^2\right]^{1/2} = \left[R_c^2 + r^2 + 2R_c r\cos(4\pi\omega t)\right]^{1/2} \\ &\equiv \left[R_c^2 + r^2 + 2R_c r\cos(2\varphi)\right]^{1/2}. \end{aligned} \tag{18}$$

To determine the kinetic energy of the ball motion transferred at impact to the particles of the powder being milled, one should know the ball velocity V. Given that the ball coordinates at time t are described by a set of equations (15), velocity V in the scalar form can be found as

$$\begin{aligned} V(t) &= \left[\left(\frac{\mathrm{d}X}{\mathrm{d}t}\right)^2 + \left(\frac{\mathrm{d}Y}{\mathrm{d}t}\right)^2\right]^{1/2} \\ &= 2\pi\omega\left[R_c^2 + r^2 - 2R_c r\cos(4\pi\omega t)\right]^{1/2} \\ &\equiv 2\pi\omega\left[R_c^2 + r^2 - 2R_c r\cos(2\varphi)\right]^{1/2}, \end{aligned} \tag{19}$$

where the angular velocity ω is expressed through the number of revolutions per unit time and $\varphi = 2\pi\omega t$. It follows from (19) that ball velocity $V(t)$ is a periodic variable depending on the rotation angle φ. Velocity $V(t)$ is directed tangentially to the motion path and changes in value and direction; it accounts for the appearance of two acceleration components, i.e., tangential a_τ and normal a_n. The former characterizes the rate of velocity changes during motion and equals $a_\tau = \mathrm{d}V(t)/\mathrm{d}t \equiv \mathrm{d}V(\varphi)/\mathrm{d}\varphi$, while the latter is perpendicular to the velocity vector and equals $a_n(t) = V^2(t)/R(t)$ in absolute value if expressions (18) and (19) are taken into account:

$$a_n(t) = \frac{V^2(t)}{R(t)} = 4\pi^2\omega^2\frac{R_c^2 + r^2 - 2R_c r\cos(2\varphi)}{\left[R_c^2 + r^2 + 2R_c r\cos(2\varphi)\right]^{1/2}}. \tag{20}$$

A milling ball of mass m moves with velocity $V(t)$ along an elliptic trajectory with the instantaneous radius $R(t)$; taking account of expressions (18) and (19), it exerts the force

$$\begin{aligned} f(t) &= ma_n(t) = \frac{mV^2(t)}{R(t)} \\ &= 4\pi^2 m\omega^2\frac{R_c^2 + r^2 - 2R_c r\cos(2\varphi)}{\left[R_c^2 + r^2 + 2R_c r\cos(2\varphi)\right]^{1/2}} \end{aligned} \tag{21}$$

on the bowl wall or a powder particle.

The maximum, mean, and minimal values of the force $f(t)$ exerted by a ball with mass $m = 0.00025$ kg at the maximum angular rotation rate (10 rps in a PM-200 Retsch mill) are 0.179, 0.089, and 0.028 N, respectively. The maximum angular rotation rate in a RITSCH Pulverisette-7 mill is 18.33 rps. Therefore, the maximum, mean, and minimal values of force $f(t)$ exerted by a ball with mass $m = 0.00022$ kg and diameter $d = 0.003$ m are 0.526, 0.239, and 0.057 N, respectively. As the ball collides with a particle of the initial powder having a mean linear size D_{in}, the particle experiences pressure $P \sim f(t)/D_{in}^2$. In such a case, the mean and maximum values of pressure P exerted on a particle with linear size $D_{in} = 10$ μm during ball milling in the PM-200 Retsch mill at a rotation speed of 10 rps are ~ 0.9 and ~ 1.8 GPa, respectively. In the RITSCH Pulverisette-7 mill with a rotation velocity of 18.33 rps, the mean and maximum values of pressure P exerted on a particle with linear size $D_{in} = 10$ μm are ~ 2.4 and ~ 5.3 GPa, respectively, if milling balls with mass $m_1 = 0.00022$ kg and diameter $d_1 = 0.003$ m are used. The impact application of calculated pressures is sufficient for grinding hard particles. As the powder undergoes fragmentation, both the number of particles in the region of point impact contact with a milling ball and the area of this region increase, which leads to a decrease in pressure P and gradual cessation of the milling.

During a single disk revolution, a milling ball covers a path equaling the ellipse perimeter length $p = 4(R_c + r)\mathbf{E}(e)$, where $\mathbf{E}(e)$ is the complete elliptic integral of the second kind for an ellipse with eccentricity $e = 2\sqrt{R_c r}/(R_c + r)$. Taking into account the series expansion of $\mathbf{E}(e)$ yields

$$p = 2\pi(R_c + r)\left[1 - \left(\frac{1}{2}\right)^2 e^2 - \left(\frac{1\cdot 3}{2\cdot 4}\right)^2 \frac{e^4}{3} - \left(\frac{1\cdot 3\cdot 5}{2\cdot 4\cdot 6}\right)^2 \frac{e^6}{5} - \ldots\right]. \quad (22)$$

Confining oneself to the first terms of the expansion leads to

$$p \approx 2\pi R_c \frac{64 - 3(r/R_c)^4}{64 - 16(r/R_c)^2}. \quad (23)$$

For the PM-200 Retsch mill, $R_c = 0.075$ m and $r = 0.0225$ m; hence, perimeter p of the elliptic trajectory equals 0.482 m. For the RITSCH Pulverisette-7 mill with $R_c = 0.065$ m and $r = 0.023$ m, the perimeter of the elliptic trajectory is 0.422 m. The total path covered by a milling ball for time t is $p\omega t$.

Force $f(t)$ acting on a milling ball is a periodic function (21). The kinetic energy of a single ball can be written as

$$E_1(t) = \int f(t)V(t)\,\mathrm{d}t = \int \frac{mV^2(t)}{R(t)}\,V(t)\,\mathrm{d}t = 8\pi^3 m\omega^3 \int \frac{\left[R_c^2 + r^2 - 2R_c r\cos(4\pi\omega t)\right]^{3/2}}{\left[R_c^2 + r^2 + 2R_c r\cos(4\pi\omega t)\right]^{1/2}}\,\mathrm{d}t. \quad (24)$$

The integral expression in function (24) cannot be represented in the explicit analytical form; therefore, the kinetic energy of a single ball was approximately presented in Ref. [36] taking into account Eqn (23):

$$E_1(t) = f_{av} p\omega t, \quad (25)$$

where $f_{av} = mV_{av}^2/R_{av} = 4\pi^2 m\omega^2(R_c^2 + r^2)^{1/2}$ is the mean centrifugal force f acting on a single ball with mass m, $V_{av} = 2\pi\omega(R_c^2 + r^2)^{1/2}$, and $R_{av} = (R_c^2 + r^2)^{1/2}$. Assuming the kinetic energy $E(t)$ of all N_b balls to be the sum of kinetic energies of individual balls yields

$$E(t) = N_b f(t) p\omega t = 8\pi^3 N_b m\omega^3 R_c \frac{64 - 3(r/R_c)^4}{64 - 16(r/R_c)^2} R(t)t, \quad (26)$$

where ω is the angular rotation rate (rps) and t is the milling time. Replacement of the instantaneous radius of trajectory $R(t)$ with the mean value $R(t) \approx R_{av} = (R_c^2 + r^2)^{1/2}$ in [36] resulted in

$$E(t) = 8\pi^3 N_b m\omega^3 (R_c^2 + r^2)^{1/2} R_c \frac{64 - 3(r/R_c)^4}{64 - 16(r/R_c)^2}\, t. \quad (27)$$

A major part of the energy is consumed during fragmentation and milling to cause elastic deformation of the milling system, i.e., to the interaction of milling bodies with the walls of the milling chamber; less than 3–5% of the total kinetic energy is spent for powder grinding [28, 29, 35, 36], making it possible to define the milling energy E_{mill} as $E_{mill} = a_k E(t)$ [34–37], where $a_k \ll 1$ is the coefficient indicating what part of the energy is consumed to grind the powder. It follows from (27) that the energy spent on powder grinding under identical conditions is proportional to the cube of the rotation angular velocity ω^3 and the duration of milling t, i.e.,

$$E_{mill} = \kappa\omega^3 t, \quad (28)$$

where

$$\kappa = 8\pi^3 a_k N_b m (R_c^2 + r^2)^{1/2} R_c \frac{64 - 3(r/R_c)^4}{64 - 16(r/R_c)^2}$$

is a constant parameter characteristic of a given mill with dimensions R_c and r, ω is the angular speed of mill rotation (rps), R_c is the radius of the circle around which the grinding bowl axis moves, r is the internal radius of the bowl, N_b is the number of milling balls, m is the mass of each ball, and a_k is the efficiency coefficient defining the part of the energy consumed to grind the powder. For the PM-200 Retsch mill, $R_c = 0.075$ m, $r = 0.0225$ m, and the total mass of the milling balls $N_b m = 0.1$ kg. Studies on the milling of niobium and tantalum carbides identified the efficiency coefficient $a_k = 0.009$ [72]; taking it into consideration gave $\kappa \approx 0.00135$ kg m^2. For the RITSCH Pulverisette-7 planetary ball mill, $R_c = 0.065$ m and $r = 0.023$ m; for the same mass of the milling balls $N_b m = 0.1$ kg at $a_k = 0.009$, coefficient $\kappa \approx 0.001032$ kg m^2, i.e., somewhat smaller than κ for the PM-200 Retsch mill. Although the grinding mechanics in PM-200 Retsch and RITSCH Pulverisette-7 are virtually identical, the use of these mills revealed a difference arising from the heating of powder-containing bowls during milling. The design of the PM-200 Retsch mill ensures excellent heat removal, due to which the bowl temperature does not exceed 340–350 K even after prolonged (10–15 h) milling at an angular rotation speed of 8.33 rps. The removal of heat in the RITSCH Pulverisette-7 mill is much less efficient, which accounts for the rapid heating of the bowls within 15–20 min at the same loaded mass and rotation speed.

The theoretical dependence of the mean particle size D on the milling time t and the mass of the ball-milled substance was obtained in [35–36] as exemplified by tungsten carbide WC. To compare the model with experiment, the authors investigated the ball milling of coarse-grained WC with the mean particle size $D_{in} \approx 6$ μm.

2.2 Comparison of the milling model and experiment with tungsten carbide (WC)

Hexagonal (space group $P\bar{6}m2$) tungsten carbide with the unit cell constants $a = 0.29060$ and $c = 0.28375$ nm has density $d_d = 15.8$ g cm^{-3}, bulk modulus $K_c = 630$ GPa, shear modulus $G = 274$ GPa, ultimate compressive strength $\sigma_c \approx 2.7$ GPa, and Poisson coefficient $\nu = 0.31$ [73, 74]. A fracture begins after the maximum microstrain $\varepsilon_{max} = \sigma_{max}/E$, equalling the ratio of the critical stress σ_{max} to the substance strength at a given deformation form is attained (E is the respective elastic modulus). Taking this into account, the limiting value of microstrains for WC lies within the $0.0045 < \varepsilon_{max} < 0.01$ range. An electron microscopic study of dislocation formation in the case of WC plastic deformation [75] showed that its main slip system is $\{1\,0\ -1\,0\}\langle 0001\rangle$, i.e., deformation along the plane $\{1\,0\ -1\,0\}$ in the $\langle 0001\rangle$ direction. For hexagonal tungsten carbide, the area of this sliding plane $s_f = ac \approx 0.0825$ nm^2, where a and c are WC unit cell constants. Moreover, sliding in the same $\{1\,0\ -1\,0\}$

plane is possible in the $\langle 11\,-23\rangle$ and $\langle 2\,-1\,-10\rangle$ directions. Burgers vectors corresponding to the sliding in these directions equal $\mathbf{b} = \langle 0001\rangle$, $(1/3)\langle 11\,-23\rangle$, and $(1/3)\langle 2\,-1\,-10\rangle$, the absolute values for hexagonal WC being $b \approx 0.26-0.29$ nm [75].

The value of qu was estimated in [35] from the atomization energy $E_{\rm at}$. The WC unit cell contains one WC formula unit and six paired W–C bonds; therefore, the energy of a single bond $q = E_{\rm at}/6N_{\rm A}$ ($N_{\rm A}$ is the Avogadro number). Four paired W–C bonds ($u = 4$) cross the $\{1\,0\,-1\,0\}$ plane. This means that $qu = 2E_{\rm at}/3N_{\rm A}$. The atomization energy of hexagonal WC found from thermodynamic data [73, 76–78] is $E_{\rm at} = 1600 \pm 50$ kJ mol^{-1}; hence, $qu = 1.77 \times 10^{-18}$ J. Taking into consideration the values of $s_{\rm f}$, qu, G, b, ν, $d_{\rm d}$ and $f_{\rm s}/f_{\rm v} = 6$, $C = 18$, and $\beta = 100$, the constants

$$A = \frac{f_{\rm s}}{f_{\rm v}}\,\frac{qu}{s_{\rm f}d_{\rm d}}\,, \qquad B = \frac{f_{\rm s}}{f_{\rm v}}\,\frac{\beta G b\sqrt{3C}}{12\pi(1-\nu)d_{\rm d}}$$

in formula (11) for hexagonal WC equal $A = 0.008$ and $B = 0.85$ J m kg^{-1}.

In accordance with [39], taking into account $E_{\rm mill}(t) = \kappa\omega^3 t$ (28), and the dependence of microstrains ε on milling time t and substance mass M, formula (11) can be written as

$$D(t,M) = \frac{M\{A + B[\ln(D_{\rm in}/2b)]\varepsilon_{\rm max}[t/(t+\tau)][M/(M+p)]\}}{\kappa\omega^3 t + M\{A + B[\ln(D_{\rm in}/2b)]\varepsilon_{\rm max}[t/(t+\tau)][M/(M+p]\}/D_{\rm in}}\,. \tag{29}$$

At a similar rotation angular velocity ω, relation (29) assumes the form

$$D(t,M) = \frac{M\big[a_{\rm D} + b_{\rm D}\varepsilon(t,M)\big]}{t + M\big[a_{\rm D} + b_{\rm D}\varepsilon(t,M)\big]/D_{\rm in}}\,, \tag{30}$$

where

$$a_{\rm D} = \frac{A}{\kappa\omega^3} = \frac{f_{\rm s}}{f_{\rm v}}\,\frac{qu}{s_{\rm f}d_{\rm d}\kappa\omega^3}\,,$$

$$b_{\rm D} = \frac{B\ln(D_{\rm in}/2b)}{\kappa\omega^3} = \frac{f_{\rm s}\sqrt{3C}}{f_{\rm v}}\,\frac{\beta G b\ln(D_{\rm in}/2b)}{12\pi(1-\nu)d_{\rm d}\kappa\omega^3}\,,$$

$$\varepsilon(t,M) = \varepsilon_{\rm max}\,\frac{t}{t+\tau}\,\frac{M}{M+p}\,.$$

For a PM-200 Retsch mill at $\kappa \approx 0.00135$ kg m^2, angular velocity of rotation $\omega = 8.33$ rps, and initial particle size $D_{\rm in} = 6 \times 10^{-6}$ m, it follows from calculations of A and B that $a_{\rm D} = 0.01037$ m s kg^{-1} and $b_{\rm D} = 10.0999$ m s kg^{-1}.

The $D_{\rm theor}(t,M)$ dependence found in [39, 79] from formulas (29) or (30), taking into consideration the theoretical values of parameters A and B (or $a_{\rm D}$ and $b_{\rm D}$) at $\varepsilon_{\rm max} = 0.0078$, angular velocity of rotation $\omega = 8.33$ rps, and initial WC particle size $D_{\rm in} = 6000$ nm, is illustrated in Fig. 2. Evidently, the longer the milling time t, the lower the mass M of the ground powder, and the smaller the size $D_{\rm in}$ of the initial powder particles the smaller the size D of the particles after milling. The rapid reduction in particle size occurs at the initial stage of the process when milling time t is shorter than 10,000 s. If the milling is prolonged any further while mass M remains unaltered, the $D(t,M)$ dependence asymptotically tends to a certain limiting value.

For comparison of the milling model proposed in [34–36] with experiment, the authors of [39] studied the milling of a coarse-grained WC powder (mean particle size $D_{\rm in} \approx 6\,\mu$m) to the nanocrystalline state with a particle size of up to 10nm.

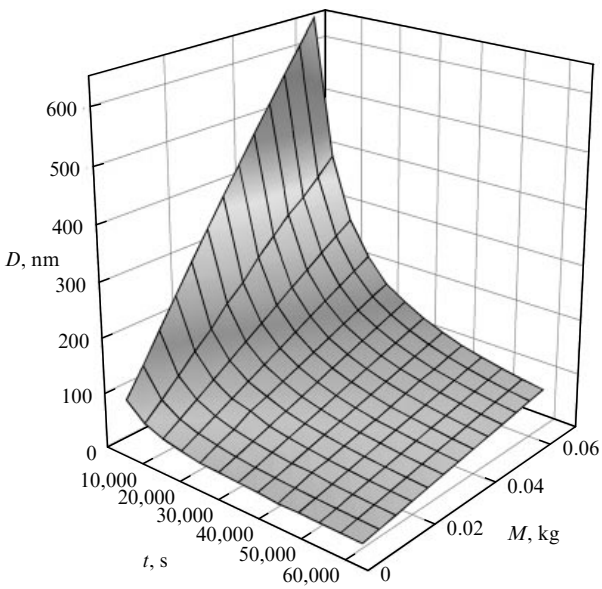

Figure 2. Theoretical three-dimensional dependence of WC particle size D on mass M of the initial tungsten carbide powder and milling time t [39, 79]. The dependence $D(t,M)$ is calculated by the formula (29) using theoretical values of A and B at $\varepsilon_{\rm max} = 0.0078$, angular velocity of rotation $\omega = 8.33$ rps, and initial particle size $D_{\rm in} = 6000$ nm.

Figure 3. PM-200 Retsch planetary ball mill.

The milling was carried out in a PM-200 Retsch mill (Fig. 3) in automatic mode with the angular velocity of rotation $\omega = 8.33$ rps and a change of direction every 15 min with 5 s stops between the changes. The total mass of $N_{\rm b} \sim 450$ milling balls was ~ 100 g. The duration of milling varied from 10 min to 15 h. 5 ml of isopropyl alcohol $CH_3CH(OH)CH_3$ was added as a milling fluid for every 10 g of the powder being ground. Compared with other suitable fluids (isobutanol, butanol, hexane, etc.), isopropyl alcohol has a higher self-ignition temperature, 729 K, and does not react with ring gaskets of the grinding bowls. The ball-milled powders were dried up. The mass of the loaded powder M taken for milling in different experiments was 10, 20, 25, and 33.3 g.

The mean size of the particles and microstrain values were determined by the diffraction method.

The initial coarse-grained WC powder contained 93.4 weight% of tungsten W and 6.6 weight% of carbon C in the absence of oxygen. The initial WC-mill powder contained 91.2 weight% of W, 5.9 weight% of C, and 2.9 weight% of oxygen O adsorbed on the surface of carbide nanoparticles. The equal relative content of W and C in the initial coarse-grained and ball-milled nanocrystalline powder suggested that the powder composition did not change during milling and remained similar to that of stoichiometric tungsten carbide WC.

X-ray diffraction patterns of the initial coarse-grained WC powder and the nanocrystalline WC-mill powder produced by grinding for 5, 10, and 15 h displayed reflections of only hexagonal WC, whereas post-milling diffraction reflections were significantly broadened. The quantitative analysis of reflection broadening in nanocrystalline WC powders showed that this was due to both the small particle size and microstrains. The size broadening was differentiated from the strain one; the size of coherent scattering regions $\langle D\rangle$ and the value of microstrains ε were determined by the Williamson–Hall method [3, 5, 80–82] using the dependence of reduced broadening $\beta^*(2\theta) = [\beta(2\theta)\cos\theta]/\lambda$ of reflections (hkl) on the scattering vector $s = (2\sin\theta)/\lambda$. The value of microstrains in relative units was found from the tilt angle φ of the straight line approximating the dependence of β^* on s using the formula $\varepsilon = \{[\beta^*(2\theta)]/2s\} \equiv [(\tan\varphi)/2]$. The value of microstrains was erroneously determined in [34–37] as $\varepsilon = \{[\beta^*(2\theta)]/4s\} \equiv [(\tan\varphi)/4]$, i.e., underestimated by a factor of 2.

When 10 g of the initial powder was taken to be ground, the mean size $\langle D\rangle$ of coherent scattering regions in WC-mill nanopowders was 32 ± 10, 20 ± 10, and 11 ± 5 nm after 5, 10, and 15 h of milling, respectively. The value of microstrains ε in the powders after grinding for 5, 10, and 15 h amounted to 0.0066 ± 0.0003, 0.0070 ± 0.0003, and 0.0060 ± 0.0004 (or $0.66 \pm 0.03\%$, $0.70 \pm 0.03\%$, and $0.60 \pm 0.04\%$).

Experimental dependences of the mean particle size D and microstrains ε in a WC powder on the milling time t and mass M of the initial powder [39] are shown in Fig. 4. The rapid decrease in particle size and growth of microstrains occurred within the first 100–150 min after the onset of milling. As the duration of milling continued to increase, dependences $D(t)$ and $\varepsilon(t)$ asymptotically approached certain limiting values. A reduction in the initial substance load M at an equal duration of milling was accompanied by a decrease in particle size and growth of microstrains.

Figure 4 shows that experimental data $D_{\text{exp}}(t, M = \text{const})$ are fairly well approximated by function (30) with parameters $a_{\text{D}} = 0.00199$ m s kg^{-1} and $b_{\text{D}} = 7.6514$ m s kg^{-1}, ε being measured in relative units. The theoretical parameters a_{D} and b_{D} are in excellent agreement with experiment. Microstrains ε (in relative units) are described by the empirical dependence $\varepsilon(t, M) = \varepsilon_{\max}[t/(t+\tau)][M/(M+p)]$, where $\varepsilon_{\max} = 0.007842$, $\tau = 7335$ s, and $p = -0.00164$ kg.

The dependence $D_{\text{theor}}(t, M = \text{const})$ (dashed line in Fig. 4a) found from (30) taking account of theoretical values of parameters a_{D} and b_{D} lies somewhat above the experimental dependence. The discrepancy between theory and experiment is attributed to the tentative estimation of quantity qu and empirical coefficients a_k, $f_{\text{s}}/f_{\text{v}}$, C, and β.

It can be concluded that investigations with the use of a coarse-grained WC powder demonstrated good agreement between theoretical and experimental dependences of the particle size on the powder mass and milling time. In accordance with the model described in [35–37], grinding of 10 g of coarse-grained WC powder for 15 h produces a nanocrystalline WC-mill powder with a mean particle size of 15 nm, the respective experimental value being $\langle D\rangle = 11 \pm 5$ nm.

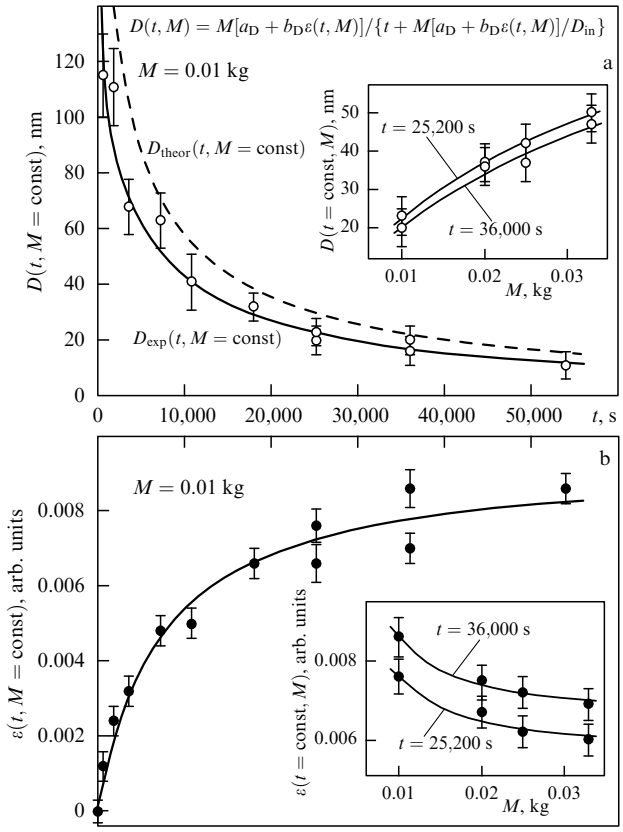

Figure 4. Dependences of (a) mean particle size D and (b) microstrains ε on the milling time t of the initial coarse-grained WC powder in a PM-200 Retsch planetary ball mill (the ball mass is 100 g, the powder mass is 10 g, the angular velocity of rotation is 8.33 rps) [39]. Calculated dependence $D_{\text{theor}}(t)$ is shown as the dashed line.

3. Peculiarities of ball milling of nonstoichiometric compounds

The overwhelming majority of solids lack homogeneity regions and a significant deviation of the composition from stoichiometry. Therefore, the model discussed in [35–37, 39] is applicable to them without corrections or additions. However, there is a group of strongly nonstoichiometric compounds with broad homogeneity regions [83–86]. They are, inter alia, cubic and hexagonal carbides, nitrides, and oxides of group IV–VI transition metals. Of special interest are carbides having extremely high hardness and refractoriness among all other solids. Nonstoichiometric carbides, especially VC_y and NbC_y, used to inhibit grain growth in hard alloys are important elements of the doped steel structure.

The influence of nonstoichiometry on the particle size in nanocrystalline powders, such as those obtained by means of ball milling, is considered in [72, 87–92].

All properties of nonstoichiometric compounds MX_y and M_2X_y (M = Ti, Zr, Hf, V, Nb, Ta; X = C, N, O) depend on their composition [83–85]. Therefore, characteristics of nonstoichiometric compounds used in milling models need to be presented as a function of their composition (relative content of a nonmetal) $y = X/M$.

The influence of nonstoichiometry on the particle size in nanocrystalline powders obtained by high energy ball milling was considered in [72, 87–92] as exemplified by nonstoichiometric titanium, niobium, and vanadium carbides MC_y having the cubic crystalline structure $B1$ and homogeneity regions of different widths. The cubic titanium and niobium carbides possess the widest homogeneity regions, ranging from $TiC_{0.48-0.50}$ to $TiC_{1.00}$ and from $NbC_{0.70}$ to $NbC_{1.00}$, respectively [84–86]. The upper boundary of the homogeneity region in cubic carbides, except vanadium carbide, is represented by stoichiometric $MC_{1.00}$ carbides. Cubic vanadium carbide has a homogeneity interval from $VC_{0.65}$ to $VC_{0.88}$ [84–86].

The main relation (11) of the high-energy ball milling model includes the coefficients

$$A = \frac{f_s}{f_v}\frac{qu}{s_f d_d}\,, \qquad B = \frac{f_s}{f_v}\frac{\beta G b\sqrt{3C}}{12\pi(1-\nu)d_d}\,,$$

characterizing a given substance and depending on its properties, where $b = |\mathbf{b}|$ is the Burgers vector magnitude, d_d, G, and ν are the density, shear modulus, and Poisson coefficient, respectively of the substance being ground, q/s_f is the number of interatomic bonds through every slip plane with area s_f per unit cell of the crystal being considered, u is the energy of a single interatomic bond of the ground substance, $f_s/f_v = 6$ is the ratio of the form factor of the volume of a particle to that of its surface area, $C = 18$ is the coefficient relating dislocation density to the microstrain value [71], and $\beta = 100$ is the coefficient taking account of the additional loss of energy for deformation of grinding bowls and milling bodies.

Formula (11) and the explicit form of coefficients A and B give evidence that the grinding of a substance with higher density d_d makes it possible, other conditions being equal, to prepare a powder with particles of a smaller size. Indeed, a high-density substance has a smaller volume V, which accounts for a higher specific milling energy E_{mill}/V. Therefore, the powder thus obtained must consist of smaller particles at the same mass M and energy E_{mill}. It is appropriate to compare the results of different studies using coarse-grained powders of different substances, such as tungsten and vanadium carbides (WC and $VC_{0.875}$) and vanadium monoxide ($VO_{1.00}$), ground in PM-200 Retsch mills under identical conditions (the angular velocity of rotation $\omega = 8.33$ rps, powder mass $M = 0.01$ kg, total mass of milling balls ~ 0.1 kg). Densities of WC, $VC_{0.875}$, and $VO_{1.00}$ are 15.8, 5.36, and 5.49 g cm^{-3}, respectively. For example, the grinding of hexagonal tungsten carbide WC for 1, 3, and 10 h produced a nanopowder with a mean particle size of 70 ± 10, 40 ± 10, and 20 ± 5 nm, respectively [35, 39]. Scanning electron microscopy showed that the mean particle size in the nanopowder of cubic vanadium monoxide VO ($V_{0.82}O_{0.82}$) obtained after 4 h of grinding was $\sim 100-120$ nm [93]. The nanocrystalline powder of cubic vanadium carbide $VC_{0.875}$ obtained by ball milling for 3 and 10 h consisted of particles with a mean size of $\sim 100 \pm 10$ and $\sim 60 \pm 10$ nm, respectively [94]. These data indicate that ball milling under comparable conditions allows producing a powder with smaller particles than those in the initial high-density substance.

3.1 Properties of nonstoichiometric compounds as a function of their composition

Because all the properties of nonstoichiometric compounds MX_y depend on their composition, the influence of nonstoichiometry on particle size in ball-milled powders has to be estimated based on the characteristics of MX_y entering in an explicit or implicit form formula (11) as functions of the relative nonmetal content $y = X/M$. These are such major characteristics as lattice constant a_{B1}, atomization energy E_{at}, shear modulus G, and Poisson coefficient ν. The length of the Burgers vector b and density d_d are related to lattice constant a_{B1}; the number of interatomic bonds q through the slip surface in the crystal of interest and the energy u of a single interatomic bond can be expressed based on the crystalline structure and the atomization energy of the substance under consideration. As a result, formula (11) can be represented in the form

$$D(y,t,M) = \frac{M\{A(y) + B(y)\varepsilon(y,t,M)\ln\left[D_{in}/2b(y)\right]\}}{E_{mill}(t) + M\{A(y) + B(y)\varepsilon(y,t,M)\ln\left[D_{in}/2b(y)\right]\}/D_{in}}\,. \tag{31}$$

Let us turn to considering nonstoichiometry taking cubic carbides MC_y as an example.

According to [35–37, 39], the energy u of a single interatomic bond can be evaluated based on the atomization energy E_{at}. In the case of cubic carbides MC_y with the $B1$-type structure, a unit cell includes 4 formula units MC_y. Therefore, the energy $4E_{at}/N_A$, where $E_{at}(y)$ is the atomization energy and N_A is the Avogadro number, corresponds to one unit cell. One unit cell of cubic carbides with the $B1$ structure includes 24 paired $M-C$ bonds, with the distance between M and C atoms equaling $a_{B1}/2$. Taking this into account, the energy u of a single interatomic bond is equal to $E_{at}(y)/6N_A$.

In cubic carbides, the movement of dislocations occurs mainly in the slip system $\{111\}\langle 110\rangle$ [95–97], i.e., $\{111\}$ planes in the $\langle 110\rangle$ direction. The sliding of close-packed atomic planes in the $\langle 110\rangle$ direction corresponds to the Burgers vector $\mathbf{b}$ with the length $b = a_{B1}\sqrt{2}/2$. It was shown in [97] that the slip plane $\{111\}$, passing through the middle of $M-C$ interatomic bonds within a cubic unit cell, has the area $s_f = (3\sqrt{3}/4)a_{B1}^2$ and crosses nine $M-C$ bonds (Fig. 5). Therefore, in the case of deformation distortion on this plane, $q/s_f = 4\sqrt{3}/a_{B1}^2(y)$. This means that $qu/s_f = 2\sqrt{3}\,E_{at}(y)/[3N_A a_{B1}^2(y)]$. The density of a cubic carbide MC_y is $d_d(y) = 4M_{MC_y}/N_A a_{B1}^3(y)$, where M_{MC_y} is its molecular mass. Because $f_s/f_v = 6$, constant A in formula (11) can be represented as

$$A = \frac{(f_s/f_v)qu}{s_f d_d} = \frac{\sqrt{3}E_{at}a_{B1}(y)}{M_{MC_y}}\,. \tag{32}$$

According to [85, 99], the atomization energy of nonstoichiometric carbides

$$E_{at}(y,298) = \Delta_s H_M^o(298) + y\Delta_s H_C^o(298) - \Delta_f H_{MC_y}^o(y,298)\,, \tag{33}$$

where $\Delta_s H^o(298)$ are the enthalpies (heats) of component vaporization and $\Delta_f H_{MC_y}^o(y,298)$ is the enthalpy of carbide MC_y formation at 298 K.

It was shown in [100] that the enthalpy of carbon (C) vaporization at 298 K $\Delta_s H_{C\,graphite}^o(298) = \Delta_s H_{C\,gas}^o(298) = 716.7$ kJ mol^{-1}. In addition, enthalpies of vaporization $\Delta_s H_M^o(298)$ were calculated in [101] for transition metals Ti, Zr, Hf, V, Nb, and Ta at 298 K. This dependences of enthalpies (heats) $\Delta_f H_{MC_y}^o(y,298)$ of formation of cubic titanium, zirconium, hafnium, vanadium, niobium, and tantalum MC_y on their composition were calculated by the

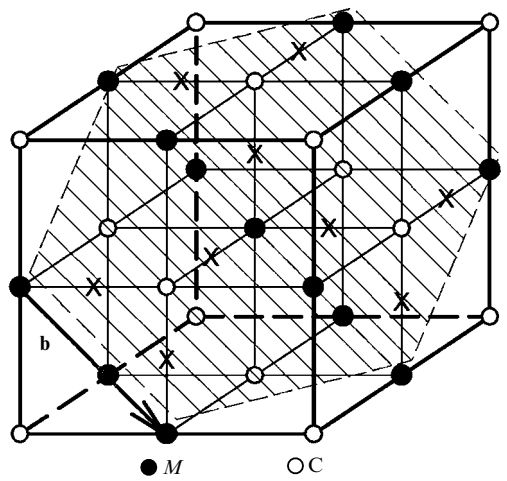

Figure 5. Slip system $\{111\}\langle 110\rangle$ in nonstoichiometric carbides MC_y with the basic $B1$ cubic structure [88, 98]. Slip on the $\{111\}$ plane breaks nine $M-C$ bonds: Xs indicate intersections of $M-C$ bonds by the slip plane, $\mathbf{b} = \langle 110\rangle/2$ is the Burgers vector indicating slip direction on the $\{111\}$ plane.

authors of [83] and reported in [84, 85]. Based on these data, the dependences of atomization energies $E_{\text{at}\,MC_y}(y, 298)$ of cubic carbides MC_y on carbon content y were calculated using formula (33) in Ref. [87].

Results of numerous experimental studies of the dependences of lattice constant $a_{B1}(y)$ on the composition of disordered titanium, zirconium, hafnium, vanadium, and tantalum carbides indicate that they are adequately described by quadratic functions $a_{B1}(y) = a_0 + a_1 y + a_2 y^2$. A more complicated composition dependence of the lattice constant $a_{B1}(y)$ is documented for disordered niobium carbide NbC_y. Functions describing the dependences of lattice constant $a_{B1}(y)$ on the composition of disordered titanium carbides (TiC_y), vanadium carbides (VC_y), and niobium carbides (NbC_y) are presented in [88].

The main slip system $\{111\}\langle 110\rangle$ [96–98] on which the movement of dislocations occurs in cubic carbides is characterized by the length of the Burgers vector $b = a_{B1}\sqrt{2}/2$. Dependences $a_{B1}(y)$ can be used to find out the dependence of the Burgers vector $b(y)$ and density $d_{\text{d}}(y)$ on the composition of MC_y carbides.

The dependences of the shear modulus G and Poisson coefficient ν on the composition y of TiC_y, VC_y, and NbC_y carbides were constructed in [88] based on experimental data borrowed from the literature. The use of the above dependences of the atomization energy $E_{\text{at}}(y)$, lattice constant $a_{B1}(y)$, Burgers vector $b(y)$, shear modulus $G(y)$, and Poisson coefficient $\nu(y)$ on the composition of disordered TiC_y, VC_y, and NbC_y carbides enabled the authors of [88] to calculate analogous dependences for constants A and B in formula (31). An analysis of formulas (11) and (31) shows that, all other conditions being equal, the lower the constants A and B, the smaller the particle size D.

The quantity $\varepsilon(t, M) = \varepsilon_{\max}[t/(t+\tau)][m/(M+p)]$ in formula (31) represents the dependence of microstrains on time t and mass $M > 0$ of a powder being ground (τ, m, and p are the normalizing parameters) [39]. The dependence $\varepsilon(t, M)$ meets the boundary conditions, because the microstrain $\varepsilon(t, M) = 0$ at $t = 0$ and $\varepsilon(t, M) \to \varepsilon_{\max}$ at $t \to \infty$. In the case of equal milling duration, the greater the value of microstrains the smaller the mass of the substance being ground. Microstrain $\varepsilon = \Delta l/l \equiv \Delta d/d$ is the relative change Δd of the interplane distance d in comparison with that in a perfect crystal. In the general case, $\Delta l/l = \sigma/E$. The fracture begins when a critical value of stress, $\sigma_{\max}$, equal to the strength of the substance at a given deformation form, is attained; therefore, $\varepsilon_{\max} = \sigma_{\max}/E$, where E is the respective shear modulus. In other words, the microstrain ε changes from zero at $t = 0$ to the limiting value $\varepsilon_{\max}$, above which the crystal lattice of the ground substance undergoes destruction. At an equal duration of milling, the greater the mass of the substance being ground, the smaller the microstrains. The ultimate value of microstrains $\varepsilon_{\max}$ falls into the $\sigma_{\text{c}}/K_{\text{c}} < \varepsilon_{\max} < \sigma_{\text{c}}/G$ range [39], where σ_{c} is compressive strength or shear strength, and K_{c} is the bulk modulus. Thus, the ultimate compressive strength depends on elastic characteristics of the substance. According to [102], the ultimate compressive strength σ_{c} of carbides is roughly $\sim G/30$ and corresponds to the stress necessary to shift one atomic plane relative to another. The Poisson coefficient of carbides ranges from 0.18 to 0.25. Taking this and $\sigma_{\text{c}} \approx G/30$ into account, the limiting value of microstrains falls into the $0.02 < \varepsilon_{\max} < 0.03$ range. The real (actual) strength of any substance, including carbides, is several times lower than $G/30$ due to defects; therefore, destruction begins at a smaller $\varepsilon_{\max}$ value. For example, $\varepsilon_{\max} = 0.008$ for tungsten carbide WC if the dependence of microstrains on milling duration and powder mass is taken into consideration [39].

The ultimate compressive strength is proportional to the energy of interatomic bonds, which, in turn, is proportional to the atomization energy E_{at} [11, 15, 24], i.e., $\sigma_{\text{c}} \sim kE_{\text{at}}$. Therefore, $\sigma_{\text{c}}(TaC_y) > \sigma_{\text{c}}(NbC_y) > \sigma_{\text{c}}(HfC_y) > \sigma_{\text{c}}(ZrC_y) > \sigma_{\text{c}}(TiC_y) > \sigma_{\text{c}}(VC_y)$, taking into account the value of $E_{\text{at}}(y, 298)$, the carbon content and all other conditions being equal. The atomization energy $E_{\text{at}}(y)$ in the homogeneity region of each carbide increases with carbon content; therefore, σ_{c} grows too with increasing y as shown in experiments [103] designed to measure the yield stress σ_{c} of titanium, zirconium, and niobium carbides. It was demonstrated in [103] that $\sigma_{\text{c}}(NbC) > \sigma_{\text{c}}(ZrC) > \sigma_{\text{c}}(TiC)$ at the same temperature.

The literature is lacking data on the influence of carbide composition on compressive and bending strains. The authors of [88], based on the analysis of concentration dependences of the atomization energy and shear modulus supplemented by the results obtained in [103, 104] on the ultimate compressive strength and yield stress of niobium carbide, presented dependences of σ_{c} and limiting values of microstrains $\varepsilon_{\max}$ on NbC_y composition as $\sigma_{\text{c}}(y) \approx 1.83 + 1.87y$ [GPa] and $\varepsilon_{\max}(y) \approx 0.0362 - 0.020y$ [rel. units], respectively. Similar dependences of σ_{c} and $\varepsilon_{\max}$ on the TiC_y and VC_y composition were described in [88] by the linear functions $\sigma_{\text{c}}(y) \approx 1.17 + 2.08y$ [GPa] and $\varepsilon_{\max}(y) \approx 0.0132 + 0.002y$ for TiC_y and $\sigma_{\text{c}}(y) \approx 1.26 + 1.87y$ [GPa] and $\varepsilon_{\max}(y) \approx 0.0209 - 0.0087y$ for VC_y, respectively.

The use of the found experimental dependences of $A(y)$, $B(y)$, $b(y)$, and $\varepsilon_{\max}(y)$ in formula (31) enabled the authors of [88–92] to analyze the influence of nonstoichiometry on the ball milling of nonstoichiometric NbC_y, TiC_y, and VC_y carbide powders.

3.2 Nonstoichiometry and particle size of carbide powders produced by ball milling

The influence of nonstoichiometry on the ball milling of a coarse-grained niobium carbide powder with a mean particle

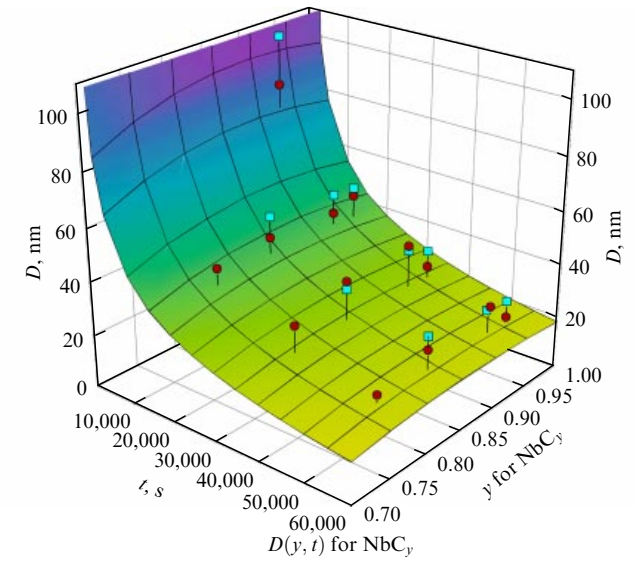

Figure 6. (Color online.) Influence of niobium carbide NbC_y composition y and milling time t on nanopowder particle size [72]. The dependence $D_{\text{theor}}(y, t)$ was calculated on the assumption of powder mass $M = 10$ g, initial particle size of 5 μm, and $E_{\text{mill}}(t) = 0.781t$ [J]. Dots and squares indicate the nanoparticle size determined by the X-ray diffraction method from diffraction reflection broadening and by the Brunauer–Emmett–Teller method, respectively.

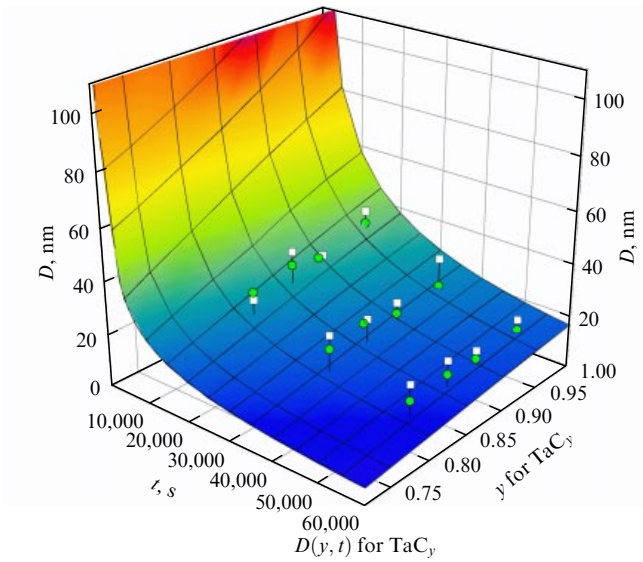

Figure 7. (Color online.) Influence of tantalum carbide TaC_y composition and milling time t on nanopowder particle size [72]. The dependence $D_{\text{theor}}(y, t)$ was calculated on the assumption of powder mass $M = 10$ g, initial particle size of 6 μm, and $E_{\text{mill}}(t) = 0.781t$ [J]. White squares and green dots indicate the nanoparticle size determined from diffraction reflection broadening and by the Brunauer–Emmett–Teller method.

size $D_{\text{in}} = 5$ μm elucidated in [72] is illustrated by Fig. 6. For comparison, the results of experimental ball milling of $NbC_{0.77}$, $NbC_{0.84}$, $NbC_{0.93}$, and $NbC_{0.96}$ powders are used. Ten grams of each powder was ground in a PM-200 Retsch mill at the angular velocity of rotation $\omega = 8.33$ rps. According to [72, 88, 90, 91], the milling energy in this mill $E_{\text{mill}}(t) = \kappa\omega^3 t \sim kt$, where $\kappa \approx 0.00135$ kg m^2; therefore, coefficient $k \sim 0.781$ J s^{-1} at $\omega = 8.33$ rps. In earlier studies [35, 36, 39, 87, 88, 94, 98], a roughly 10% overrated coefficient $\kappa = 0.0015$ kg m^2 was used to assess the milling energy. The results of calculations (see Fig. 6) are in excellent agreement with the experimental data obtained in the grinding of $NbC_{0.77}$, $NbC_{0.84}$, $NbC_{0.93}$, and $NbC_{0.96}$ powders with the initial particle size $D_{\text{in}} = 5-7$ μm for 5, 10, and 15 h.

The dependence of the particle size in TaC_y powders on nonstoichiometry and milling time is presented in Fig. 7. The mean size of the particles in initial coarse-grained tantalum carbide powders $D_{\text{in}} = 6$ μm. Its fast decrease to 100 nm or less takes 1000–2000 s. A longer duration of milling (up to 15 h or more) is associated with a slow asymptotic decrease in particle size, in agreement with the results of experiments on the ball milling of $TaC_{0.81}$, $TaC_{0.86}$, $TaC_{0.90}$, and $TaC_{0.96}$ powders for 5, 10, and 15 h. Theoretical dependences $D(y)$ for TaC_y at a fixed milling time t, unlike those for niobium carbide, are smooth and display no maxima (see Fig. 7). This difference is attributed to the rather smooth dependences of the lattice constant $a_{B1}(y)$, shear modulus $G(y)$, and coefficient $B(y)$ of TaC_y. The somewhat smaller theoretical particle size $D(y, t)$ of tantalum carbide than the experimental one can be accounted for by the use of the underestimated TaC_y shear modulus G in calculations, taking into consideration that the measurements of elastic characteristics described in the literature were performed on porous samples.

The theoretical dependence of the particle size D of a nonstoichiometric VC_y powder on the milling time t and VC_y composition calculated in [88] is presented in Fig. 8. Calculations show that the mean particle size is 20–25 nm when milling lasts 15 h. A change in the VC_y composition at the same milling duration only slightly affects the particle size in the resulting powder due to the almost linear variation in shift $G(y)$ and parameter $B(y)$, depending on carbide composition. A diffraction experiment showed that the mean size $\langle D \rangle$ of coherent scattering regions in a $VC_{0.875}$ nanopowder obtained in 10 h of milling varies from 40 to 80 nm at the same microstrain value. The theoretical estimate of the particle size in the $VC_{0.875}$ nanopowder produced by ball milling for

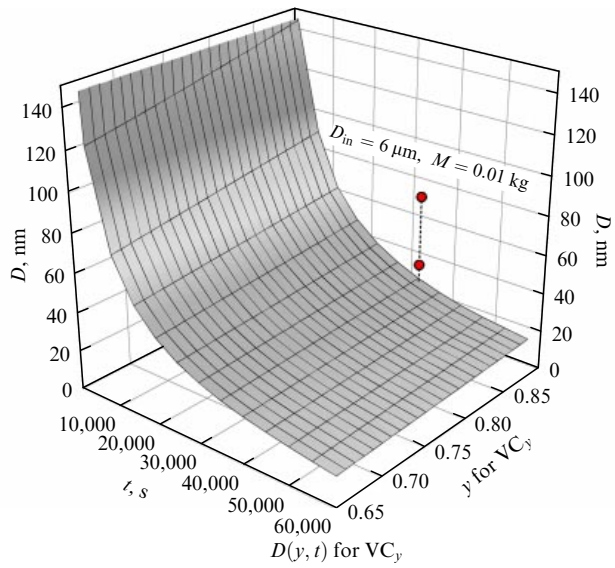

Figure 8. Model dependence $D(y, t)$ of vanadium carbide VC_y powder particle size on carbon content y and milling time t [88]. Mass M of initial powder is 10 g, initial particle size is 6 μm. The dependence $D(y, t)$ was calculated for $E_{\text{mill}}(t) = 0.868t$ [J]. The dots show experimental particle size of $VC_{0.875}$ powder after 10 h of milling.

10 h is lower (32 nm) because calculations in [88] were made based on the underestimated experimental data from the literature on vanadium carbide shear modulus G measured on porous samples. Indeed, it follows from formulas (11) and (31) that a greater particle size obtained by ball milling corresponds to a higher shear modulus. Another cause of theoretical underestimation of the particle size in the VC_y powder is the overrated milling energy $E_{\text{mill}}(t) = 0.868t$ [J] used in [88]. Actually, $E_{\text{mill}}(t) = 0.781t$ [J], as was shown in a later study [72].

3.3 Ball milling of titanium, vanadium, and niobium monoxides

High-energy ball milling ensures a high concentration of energy on the particles. The authors of [93, 105–109] used a Retsch PM-200 mill with grinding bowls and balls made from yttrium oxide-stabilized zirconium dioxide to disintegrate nonstoichiometric titanium, vanadium, and niobium oxides containing tens of percent of structural vacancies in both oxygen and metal sublattices. The mass ratio of the grinding bowls and balls was 10:1. Isopropyl alcohol served as the milling fluid.

Production of a nanocrystalline vanadium monoxide $VO_{1.0}$ powder with a type $B1$ cubic structure is described in Refs [93, 105, 106]. The duration of milling was 15 min to 4 h, with a change of rotation direction every 15 min. The ball-milled vanadium monoxide retained the cubic structure but experienced broadening of all diffraction reflections. The size of coherent scattering regions that can be regarded as the nanoparticle size varied from ~ 310 to ~ 20 nm with a rise in the milling duration from 15 min to 4 h. High-resolution electron microscopy demonstrated that particles of the VO nanopowder obtained by 4 h of ball milling were 20–30 nm in size. In other words, results of the measurement of VO particle size by electron microscopy and X-ray diffraction techniques are in good agreement.

The influence of nanoparticle size on the stability of composition and structural vacancies in nanocrystalline titanium monoxide was studied in [107, 108]. Nanopowders of titanium monoxide were prepared by grinding macrocrystalline (particle size $\sim 15-25$ μm) powders of nonstoichiometric $TiO_{0.92}$, $TiO_{0.97}$, $TiO_{0.99}$, and $TiO_{1.23}$. The initial $TiO_{0.92}$ and $TiO_{1.23}$ powders were disordered and had the type $B1$ cubic structure. The initial $TiO_{0.97}$ and $TiO_{0.99}$ powders were used in both disordered (hardened) and ordered (obtained by low-temperature annealing) states. The ordered $TiO_{0.97}$ and $TiO_{0.99}$ monoxides had the Ti_5O_5 type monoclinic structure (space group $C2/m$). The duration of initial powder milling at an angular rotation speed of the bearing disk of 500 rpm (8.33 rps) was 15, 30, 60, 120, 240, and 480 min, with the rotation direction reversed every 15 min. The ball-milled titanium monoxides retained the initial composition and crystalline structure, but diffraction reflections markedly broadened (Fig. 9).

The broadening became apparent within 15 min after the onset of the milling. However, such short-term grinding was incomplete and the powders contained components of the initial coarse-crystalline fraction. It took 4 h to obtain samples composed of nanocrystalline particles alone.

An analysis of broadening of diffraction reflections showed that the particle size in the nanopowder of annealed $TiO_{0.99}$ obtained in 8 h of milling was roughly 20 nm, while the value of microstrains amounted to 0.57%. The dependence of the mean particle size D on milling time t was approximated

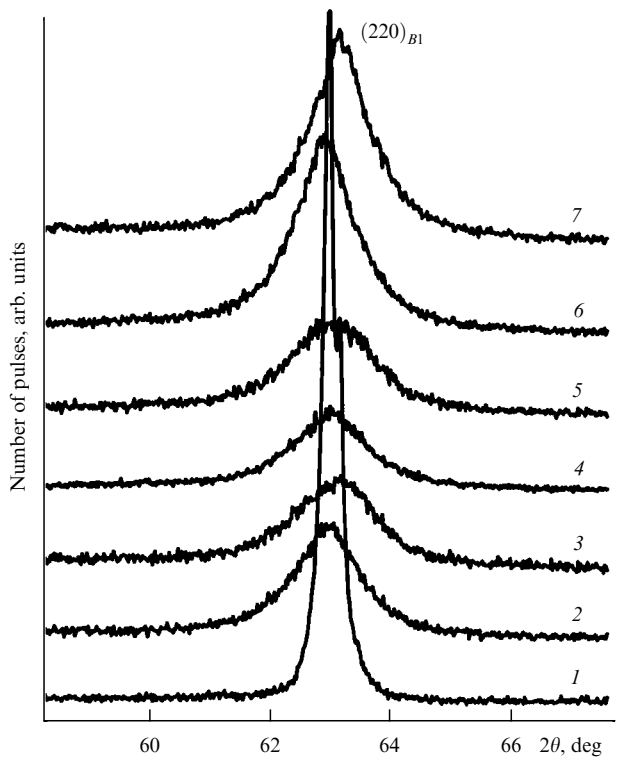

Figure 9. Diffraction reflections $(220)_{B1}$ (*1*) from initial coarse-crystalline disordered $TiO_{0.99}$ powder and (*2–7*) TiO_y nanopowder obtained after 8 h of milling [108]: (*2*, *3*) disordered hardened and ordered annealed $TiO_{0.99}$ nanopowders; (*4*, *5*) disordered hardened and ordered annealed $TiO_{0.97}$ nanopowders; (*6*, *7*) disordered hardened $TiO_{0.92}$ and $TiO_{1.23}$ nanopowders, respectively.

in [107] by the hyperbolic function

$$D(t) = \frac{D_{\text{in}} - D_{\text{min}}}{1 + ct} + D_{\text{min}}\,, \tag{34}$$

where $D_{\text{min}} = 20 \pm 10$ nm is the minimal particle size attainable by milling and c is the coefficient related to the milling energy and fragility of the material (the totality of its strength characteristics, to be precise). The particle size in nanopowders of ordered titanium monoxide is 3–5 nm smaller than in disordered monoxides. The general dependence of the size of the coherent scattering region (CSR) on the TiO_y nanopowder composition obtained after 8 h milling is described in [108] by the linear function $D(y) = 69.3y - 49.4$ [nm]. Electron microscopy revealed rounded particles 20–30 nm in size in nanopowders produced by milling for 8 h. Moreover, an aggregation of nanoparticles with the formation of 40–300 nm polycrystals was observed.

Cubic (space group $Pm\bar{3}m$) niobium monoxide NbO has an unusual structure containing 25 at.% vacancies in sublattices of both niobium and oxygen but lacks a homogeneity region [84–86, 110]. A coarse-crystalline niobium monoxide powder was synthesized in [109] by solid-phase vacuum sintering of a mixture of metallic niobium Nb and niobium oxide Nb_2O_5 at 1673 K for 24 h. Then, the NbO thus obtained was annealed in a vacuum at 1773 and 1873 K. The resulting single-phase NbO powder with a cubic structure (space group $Pm\bar{3}m$) had a lattice constant of 0.4212 nm. The macrocrystalline NbO powder was ground in a Retsch PM-200 mill for 30, 60, 120, 240, and 480 min [109]. Isopropyl alcohol and surface active agents (SAAs), such as PEG-400 polyethylene

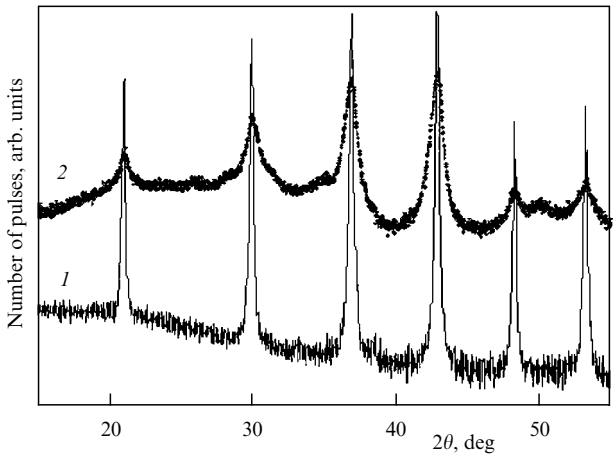

Figure 10. X-ray diffraction patterns of niobium monoxide NbO powders in the initial state (*1*) and ground for 8 h (*2*).

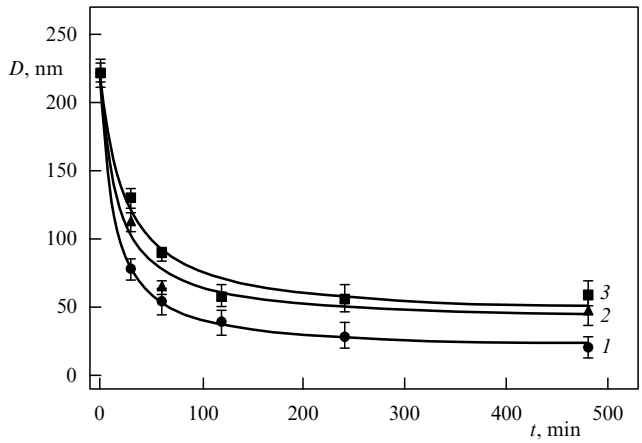

Figure 11. Dependences of CSR of niobium monoxide powders on the duration of grinding with different milling fluids: (*1*) isopropyl alcohol, (*2*) PEG-400, (*3*) PEG-400 + $(C_4H_9)_4N^+I^-$ [109].

glycols and PEG-400 containing diluted tetrabutylammonium iodide $(C_4H_9)_4N^+I^-$, were used as the milling fluids. SAAs served to disengage fragmented particles after milling, i.e., to create a stable aqueous suspension of niobium monoxide.

X-ray diffraction patterns of the initial and ball-milled (8 h) niobium monoxide powders are presented in Fig. 10. Diffraction reflections of the initial powder are narrow and split into $\alpha_{1,2}$ doublets, which suggests a high degree of NbO homogeneity. XRD patterns of the ground nanopowders display the same but markedly broadened diffraction reflections. Analysis of the dependence of reduced broadening of diffraction reflections showed that the broadening is attributable to both the small particle size and the presence of microstrains. Also, the authors of [109] observed anisotropy of nanocrystal size in directions [100], [110], and [111], with NbO nanocrystals having a smaller size in direction [100] than in [110] and [111].

The CSR size of the nanopowder obtained by milling for 8 hr with the use of isopropyl alcohol as the milling fluid decreased from 200 to 20 nm, while the value of microstrains amounted to 0.36%. When PEG-400 and PEG-400 + $(C_4H_9)_4N^+I^-$ were used as the milling fluids, the CSR size decreased only to 40 nm and the microstrain value increased to 0.2%. The dependence of the CSR size on milling time t had a hyperbolic form (Fig. 11). Milling in isopropyl alcohol, with all other conditions being equal, produced the finest nanopowder. Electron microscopy revealed rounded and lamellar NbO nanoparticles 20–30 nm in size coalescing to form 40–300 nm polycrystals. TiO_y and NbO nanopowders obtained by ball milling under the identical conditions in [107–109] had a similar microstructure.

4. Microstructure of carbide nanopowders prepared by high-energy ball milling

Grinding results not only in a decrease in particle size, i.e., fragmentation, but also in the appearance of microstrains. X-ray and neutron diffraction techniques provide a powerful tool for the study of nanocrystalline substances with special reference to the particle size (coherent scattering regions) and microstrains. Electron microscopy and laser diffraction are used as supplementary methods to confirm findings obtained by diffraction methods.

P Scherrer was the first to propose the application of X-rays to determine the particle size. In 1918, he derived a formula relating the diffraction reflection width at its half-height to the particle size of the substance under study [111]. An analogous relation was reported in a later paper [112] by the Soviet researcher N Ya Selyakow.

It readily follows from the Wulff–Bragg condition that $\Delta d_{hkl}/d_{hkl} = -\cot(\theta_{hkl})\Delta\theta$; on the other hand, $\Delta d_{hkl}/d_{hkl} = \Delta\lambda/\lambda$; therefore, $\Delta\lambda/\lambda = -\cot(\theta)\Delta\theta$, whence broadening $\beta_{hkl}(2\theta) = |-2(\Delta\lambda/\lambda)\tan\theta_{hkl}| = 2(\Delta\lambda/\lambda)\tan\theta_{hkl}$. This expression can be used to determine the maximum size of particles (grains, crystallites) responsible for a measurable broadening of reflections on the assumption that the minimal width is equal to the spectral width of reflection $\Delta\lambda/\lambda \approx 10^{-3}$. In this case, the broadening $\beta_{hkl} = 2\times10^{-3}\tan\theta_{hkl}$ and

$$\langle D\rangle = \frac{\lambda}{\beta_{hkl}\cos\theta_{hkl}} = \frac{10^3\lambda}{2\tan\theta_{hkl}\cos\theta_{hkl}} = \frac{10^3\lambda}{2\sin\theta_{hkl}} = 10^3 d_{hkl} \approx 200\ \text{nm}\,.$$

This means that the diffraction method allows the size of particles smaller than 200 nm to be determined.

In general, when particles have an arbitrary shape, their mean size $D_{\text{av}} \approx V^{1/3}$ (V is particle volume) can be found using the Debye–Scherrer formula [3, 5, 111]:

$$\langle D\rangle = \frac{K_{hkl}\lambda}{\cos\theta\,\text{FWHM}_{\text{exp}}(2\theta)} \equiv \frac{K_{hkl}\lambda}{2\cos\theta\,\text{FWHM}_{\text{exp}}(\theta)}\,, \qquad (35)$$

where λ is the radiation wavelength and $K_{hkl} \approx 1$ is the Scherrer constant (anisotropy coefficient), whose value depends on the particle (crystallite, domain) shape and diffraction reflection indices (hkl).

In a real experiment, the reflection broadens as a result of finite resolution of the diffractometer and cannot be smaller than the instrumental linewidth. This implies the necessity to use in formula (35) broadening β of reflection with respect to instrumental width FWHM_{R} rather than experimental reflection width $\text{FWHM}_{\text{exp}}(2\theta)$:

$$\beta(2\theta) = \left[(\text{FWHM}_{\text{exp}})^2 - (\text{FWHM}_{\text{R}})^2\right]^{1/2}. \qquad (36)$$

Formula (36) should be used if the physical broadening β and the instrumental width $\mathrm{FWHM_R}$ are described by the Gaussian or pseudo-Voigt functions, with a greater contribution from the former. As a matter of practice, such a description of the experimental broadening and the diffractometer resolution function is most widely used. If both the physical broadening and the instrumental width are described by the Lorentz (Cauchy) functions, the physical broadening equals the difference between the total experimental reflection width and the instrumental reflection width, i.e., $\beta = \mathrm{FWHM_{exp}} - \mathrm{FWHM_R}$.

According to [113], the diffraction reflection broadening due to the small particle size (size broadening) equals

$$\beta_{\mathrm{s}}(2\theta) = \frac{K_{hkl}\lambda}{\langle D\rangle \cos\theta} \approx \frac{\lambda}{\langle D\rangle \cos\theta} \ \ [\mathrm{rad}]\,, \tag{37}$$

while broadening caused by deformation distortions of the crystal lattice (strain broadening) equals

$$\beta_{\mathrm{d}}(2\theta) = 4\varepsilon \tan\theta \ \ [\mathrm{rad}]\,. \tag{38}$$

The mean particle size D_{av} is determined in a diffraction experiment by the Warren method [82] taking (37) into account:

$$\langle D\rangle = \frac{K_{hkl}\lambda}{\cos\theta\,\beta_{\mathrm{s}}(2\theta)} \equiv \frac{K_{hkl}\lambda}{2\cos\theta\,\beta_{\mathrm{s}}(\theta)}\,. \tag{39}$$

Notice that $\beta(2\theta) = 2\beta(\theta)$.

The broadening in nanostructured materials is as a rule due to both the small particle size and microstrains. To separate these two contributions to the experimental reflection broadening, the extrapolation Williamson–Hall method [80] is used. It is based on the construction of the dependence of the reduced broadening $\beta^*(2\theta) = [\beta(2\theta)\cos\theta]/\lambda$ of diffraction reflections (hkl) on the scattering vector $s = (2\sin\theta)/\lambda$. The Williamson–Hall method is based on the assumption that size and strain broadenings are described by the Lorentz (Cauchy) functions. As a result, the total reflection broadening is the sum of size and strain broadenings, i.e., $\beta(2\theta) = \beta_{\mathrm{s}}(2\theta) + \beta_{\mathrm{d}}(2\theta)$ or, taking account of (37) and (38), $\beta(2\theta) = \beta_{\mathrm{s}}(2\theta) + \beta_{\mathrm{d}}(2\theta) = \lambda/(\langle D\rangle\cos\theta) + 4\varepsilon\tan\theta$. Then, the reduced broadening $\beta^*(2\theta) = [\beta(2\theta)\cos\theta]/\lambda$ as a function of scattering vector s equals $\beta^*(2\theta) \equiv \beta^*(s) = 1/\langle D\rangle + 2\varepsilon(2\sin\theta)/\lambda = 1/\langle D\rangle + 2\varepsilon s = 1/\langle D\rangle + s\tan\varphi$, where $2\varepsilon \equiv \tan\varphi$ and φ is the slope angle of the straight line approximating the $\beta^*(s)$ dependence and a linear function of the scattering vector s.

The mean particle size $\langle D\rangle$ is determined in the Williamson–Hall method by extrapolating the dependence of the reduced broadening $\beta^*(2\theta)$ on the scattering vector s to the value $s = 0$, i.e., $\langle D\rangle = 1/\beta^*(2\theta)|_{s=0}$, and the mean value of microstrains $\varepsilon_{\mathrm{av}}$ is found from the slope angle φ of the straight line approximating the dependence $\beta^*(s)$ as $\varepsilon_{\mathrm{av}} = [(\tan\varphi)/2]100\%$. The Williamson–Hall method should be used if reflection broadening β is described by the Lorentz function or the pseudo-Voigt function with a large (at least 70%) contribution from the Lorentz function.

The physical sense of quantity $\varepsilon = \Delta d/d$ is a lattice microstrain characterizing uniform deformation averaged over the entire crystal volume, i.e., a relative change in the interplane distance in comparison to that in a perfect crystal (d and Δd are the interplane distance in the perfect crystal and the mean change in the interplanar distance (hkl) in the crystal bulk, respectively).

Usually, the broadening $\beta_{\mathrm{d}}(2\theta)$ caused by deformation distortions of the lattice is represented in the form (38). However, microstrain anisotropy needs to be taken into consideration in strongly deformed substances, such as nanopowders obtained by high-energy ball milling. According to [82, 114], the broadening $\beta_{\mathrm{d}}(2\theta)$ caused by anisotropic deformation distortions of the crystal lattice equals

$$\beta_{\mathrm{d}}(2\theta) = 4\varepsilon_{hkl}\tan\theta \ \ [\mathrm{rad}]\,, \tag{40}$$

where $\varepsilon_{hkl} = \sigma/E_{hkl} = k_\rho C_{hkl}^{1/2}$ is the effective microstrain taking into account strain anisotropy of the crystal, σ is the direction-independent full width at half-maximum of the stress distribution function, E_{hkl} is the $[hkl]$-dependent Young's modulus, and k_ρ is a constant for a given sample depending on dislocation density and the Burgers vector, i.e., on the change in interplanar spacing and atomic displacements. In the theory of elasticity, anisotropic Young's modulus E_{hkl} of cubic crystals is defined by elastic constants c_{11}, c_{12}, and c_{44} or components s_{11}, s_{12}, and s_{44} of the elastic deformation tensor as

$$E_{hkl} = \frac{1}{s_{11} - (2s_{11} - 2s_{12} - s_{44})H}\,, \tag{41}$$

where $H = (h^2k^2 + k^2l^2 + h^2l^2)/(h^2 + k^2 + l^2)^2$ is the dislocation anisotropy factor for cubic crystals [115]. Coefficient C_{hkl} takes account of edge and screw dislocations in a deformed crystal. According to [115], coefficient C_{hkl} for cubic crystals is

$$C_{hkl} = f_E C_{hkl,E} + (1 - f_E)C_{hkl,S} = \left[f_E A_E + (1 - f_E)A_S\right] + \left[f_E B_E + (1 - f_E)B_S\right]H = A_{\mathrm{d}} + B_{\mathrm{d}}H\,, \tag{42}$$

where f_E and $f_S = 1 - f_E$ are the relative content of edge and screw dislocations, and A_{d} and B_{d} are constants for a given sample depending on dislocation density and relative content.

Taking account of $\varepsilon_{hkl} = k_\rho C_{hkl}^{1/2}$ and (42), expression (40) can be written in the form

$$\beta_{\mathrm{d}}(2\theta) = 4k_\rho C_{hkl}^{1/2}\tan\theta \equiv 4k_\rho(A_{\mathrm{d}} + B_{\mathrm{d}}H)^{1/2}\tan\theta\,. \tag{43}$$

It follows from (42) and (43) that the anisotropy of microstrains is due to the presence of dislocations or dislocation-like defects rather than to atomic displacements.

According to [116], the value of microstrains $\varepsilon_{\mathrm{av}}$ averaged over the crystal bulk is expressed as

$$\varepsilon_{\mathrm{av}} = \frac{\sum \varepsilon_{hkl}P_{hkl}}{\sum P_{hkl}}\,, \tag{44}$$

where P_{hkl} is the repetition factor.

The use of the Williamson–Hall method and taking into consideration (37) and (43) allow describing broadening as $\beta(2\theta) = \lambda/(D\cos\theta) + 4k_\rho(A_{\mathrm{d}} + B_{\mathrm{d}}H)^{1/2}\tan\theta$ and reduced broadening as $\beta^*(2\theta) = 1/D + 2k_\rho(A_{\mathrm{d}} + B_{\mathrm{d}}H)^{1/2}s$.

The influence of milling time and the nonstoichiometry of cubic tantalum carbide TaC_y $(0.81 \leqslant y \leqslant 0.96)$ on anisotropic deformation of crystals and particle size in nanocrystalline powders was studied in X-ray diffraction experiments [91, 92]. A rise in milling duration t and energy E_{mill} was accompanied by a significant broadening of diffraction reflections due to the reduction in the particle size and growth of microstrains. As an example, Fig. 12 shows a change in microstrain value $\varepsilon_{\mathrm{av}}$ determined without regard to the anisotropy of TaC_y

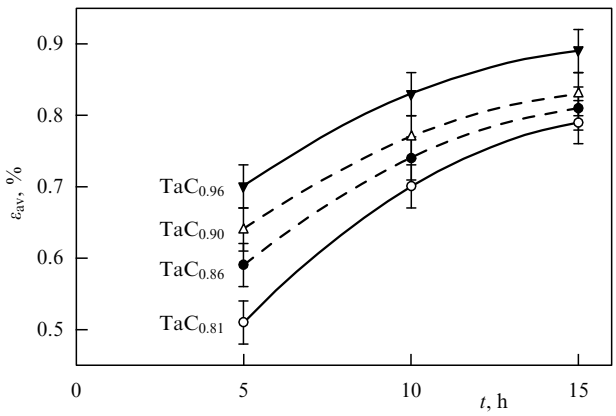

Figure 12. Mean microstrain value ε_{av} versus TaC_y powder milling time t.

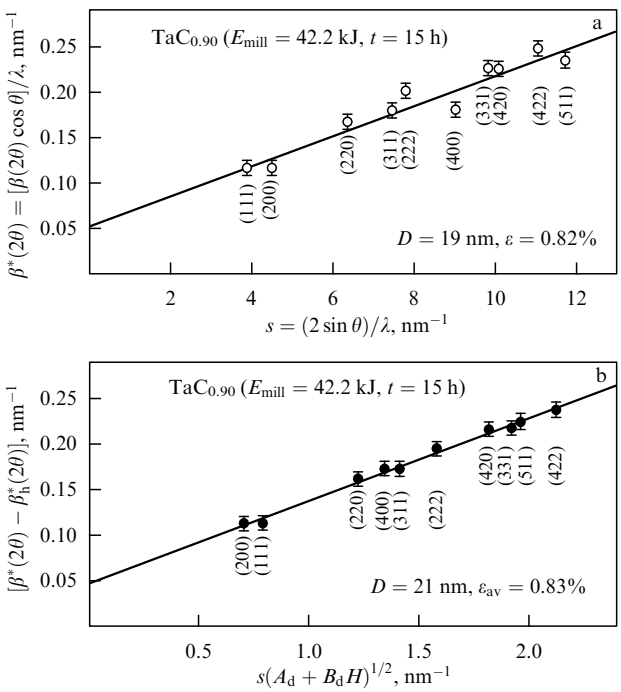

Figure 13. Reduced broadening $\beta^*(2\theta)$ of diffraction reflections from a $TaC_{0.90}$ powder obtained after 15 h of milling [92]: (a) dependence of reduced broadening on scattering vector s without regard for microstrain anisotropy; (b) dependence of reduced broadening taking account of microstrain anisotropy ε_{hkl}.

nanopowders obtained by different durations of milling t. Prolongation of milling caused a gradual growth of ε_{av}.

Experimental dependences of reduced broadening $\beta^*(2\theta)$ of diffraction reflections in a $TaC_{0.90}$ powder formed in the course of 15 h of milling are presented in Fig. 13 [92]. Experimental data points of the dependence of $\beta^*(2\theta)$ on the scattering vector s constructed without regard to microstrain anisotropy are spread with respect to the approximating linear dependence $\beta^*(s)$ (Fig. 13a). Approximation of the same experimental data by function $\beta^*(2\theta) = 1/D + 2k_\rho(A_d + B_d H)^{1/2}s$ as the dependence on $s(A_d + B_d H)^{1/2}$ (Fig. 13b) taking account of microstrain anisotropy yields a better agreement between experiment and approximating linear dependence.

According to [91, 92], the lowest value of microstrains ε_{hkl} for all TaC_y nanopowders is observed in [200] and equivalent directions, while the highest value is recorded in direction [111]. Figure 14 shows the distribution of microstrains ε_{hkl} in nonequivalent directions $[hkl]$ in $TaC_{0.81}$ powders obtained after milling for 5 and 15 h with energy $E_{mill} = 14.1$ and 42.2 kJ, respectively. The radius of the spheres is proportional to microstrain ε_{av} averaged over all crystallographic directions, and the vector length to ε_{hkl}. Evidently, in both powders, microstrains ε_{111}, ε_{220}, ε_{331}, and ε_{422} in [111], [220], [331], and [422] directions exceed the averaged microstrain ε_{av} equaling 0.51% and 0.79% for milling energies of 14.1 and 42.2 kJ, respectively.

Neutronography provides an optimal tool for simultaneous investigation of nanostructuring and possible ordering of nonstoichiometric carbides and oxides. On the one hand, comparable intensities of neutron scattering from atomic nuclei of transition metals and carbon or oxygen make it possible to detect ordering in these substances. On the other hand, the diffraction of short-wavelength neutron radiation provides an opportunity to determine the grain size in microstrains and other defects in the lattice of nanocrystalline substances.

The most promising of the tools for neutron diffraction research are time-of-flight (TOF) diffractometers on pulsed neutron sources. The use of a continuous neutron wavelength spectrum allows covering a wide range of interplane distances d_{hkl} more accurately than in a standard diffractometer with a monochromatic neutron beam, evaluating the influence of various crystal defects (small particle size, microstrains, vacancy-related nonstoichiometry) on the reflection profile and width, and detecting fractions with particles of different sizes in the sample.

Earlier studies on the influence of nonstoichiometry and small particle size on the structure of nanocrystalline substances were performed by the TOF-neutronography technique in 2014–2018 with the use of MC_y carbides [116–123].

When diffraction reflections are described by the pseudo-Voigt function with a large contribution of the Gaussian function, their broadening is the superposition of size and strain broadenings:

$$\beta^2(2\theta) = \beta_s^2(2\theta) + \beta_d^2(2\theta)\,. \tag{45}$$

Differentiation of the Wulff–Bragg equation $d = \lambda/(2\sin\theta)$ yields either $\Delta d/\Delta\theta = |d/\tan\theta|$ or $|\Delta\theta| = (\Delta d/d)\tan\theta$. Reflection broadening on both sides of the maximum corresponding to interplanar spacing d is twice that, $\beta(2\theta) = 2|\Delta\theta|$, which means that the angular broadening $\beta(2\theta)$ can be represented as the interplane distance d in the form

$$\beta(2\theta) = 2|\Delta\theta| = 2\,\frac{\Delta d}{d}\tan\theta\,. \tag{46}$$

The mean size of the coherent scattering region is related to strain broadening $\beta_s(2\theta)$ (37). Taking into consideration the Wulff–Bragg conditions and substituting λ by $2d\sin\theta$ in (37) allow the strain broadening to be written as

$$\beta_s(2\theta) = \frac{2d\sin\theta}{D\cos\theta} = 2\,\frac{d}{D}\tan\theta\,. \tag{47}$$

Substituting (43), (46), and (47) into (45) yields $(\Delta d/d)^2 = d^2/D^2 + 4\varepsilon_{hkl}^2$ or

$$(\Delta d)^2 = 4d^2\varepsilon_{hkl}^2 + \frac{d^4}{D^2} = (2k_\rho)^2(A_d + B_d H)d^2 + \frac{d^4}{D^2}$$
$$= c_3(A_d + B_d H)d^2 + c_4 d^4\,. \tag{48}$$

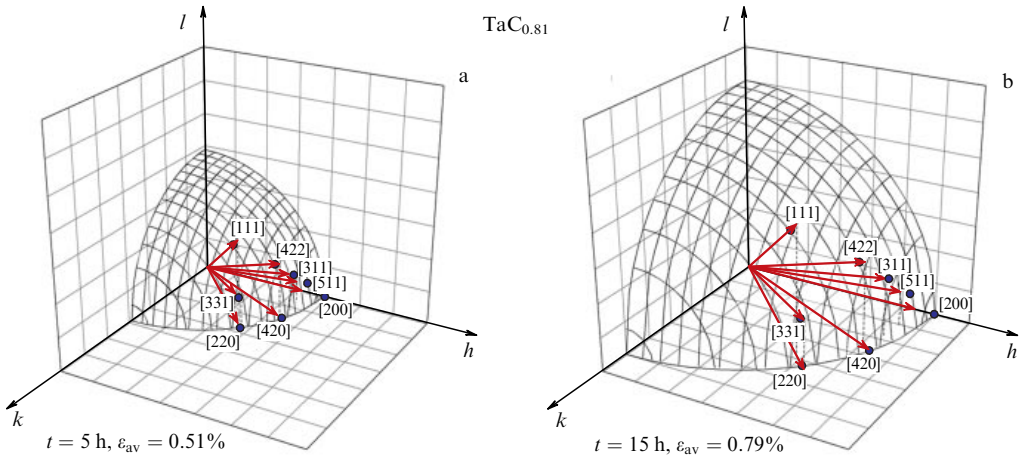

Figure 14. Distribution of microstrains ε_{hkl} in nonequivalent directions $[hkl]$ in $TaC_{0.81}$ nanopowder produced in (a) 5 and (b) 15 h of milling with energies $E_{\text{mill}} = 14.1$ and 42.2 kJ, respectively. The radius of the sphere is proportional to ε_{av}, and the vector length in directions $[hkl]$ to the value of microstrains ε_{hkl} [92].

The dependence of the diffraction reflection width Δd on interplanar distance d in a polycrystal measured with an HRFD diffractometer includes the contribution from the diffractometer resolution function W_{R} and has the form

$$(\Delta d)^2 = c_1 + c_2 d^2 + c_3(A_{\text{d}} + B_{\text{d}} H)d^2 + c_4 d^4 \,, \qquad (49)$$

where coefficients c_1 and c_2 are related to the diffractometer resolution function and parameters (flight distance, scattering angle), $c_3 \approx (2\varepsilon)^2$, and $c_4 \approx (1/D)^2$. The experimental broadening is related to Δd as $W = K\Delta d$, where for the HRFD diffractometer constant $K = 25912.7$ if Δd is measured in nanometers. Substituting Δd by W in (49) yields

$$W^2 = C_1 + C_2 d^2 + C_3(A_{\text{d}} + B_{\text{d}} H)d^2 + C_4 d^4 \,, \qquad (50)$$

where $C_i = c_i K^2$, $C_1 + C_2 d^2 = W_{\text{R}}^2$ is the square of the diffractometer resolution function W_{R}, and the third and the fourth items are the contributions from strain and size broadenings, respectively.

If the resolution function is taken into consideration, the square of the broadening

$$\beta_{hkl}^2 = W^2 - W_{\text{R}}^2 = C_3(A_{\text{d}} + B_{\text{d}} H)d_{hkl}^2 + C_4 d_{hkl}^4 \,. \qquad (51)$$

Dependence (51) constructed as a function of d^2 is either a concave curve or a straight line because, by definition, $C_4 = K^2(1/D^2) \geqslant 0$ and $C_3 = K^2(2\varepsilon)^2 \geqslant 0$. Taking account of anisotropy, the microstrain ε_{hkl} has the form $\varepsilon_{hkl} = 1/2[C_3(A_{\text{d}} + B_{\text{d}} H)]^{1/2}$.

As is mentioned in a preceding paragraph, the main causes of diffraction reflection broadening are the small size D of particle or crystallite coherent scattering regions and microstrains ε in the crystal lattice due to its deformation distortions and atomic displacements associated with the presence of dislocations [124]. Taking account of the microstrain value and anisotropy is of special importance as far as strongly deformed substances and materials such as ball-milled carbide nanopowders are concerned [125–128].

TOF neutron diffraction was used in [119, 122] to study the evolution of the microstructure of nonstoichiometric vanadium carbide V_8C_7 ($VC_{0.875}$) prepared by high-energy ball milling.

Neutron diffraction patterns of coarse-crystalline and nanocrystalline vanadium carbide powders V_8C_7 ($VC_{0.875}$) are presented in Fig. 15. The large d_{hkl} spectral region of the coarse-crystalline $\sim V_8C_7$ powder (Fig. 15a) contains weaker superstructure reflections of the V_8C_7 cubic (space group $P4_332$) ordered phase. Considerable broadening accounts for less apparent superstructure reflection in the spectrum of a nanopowder obtained after 10 h of milling (Fig. 15b). The wide peak visible in the $d \sim 0.185-0.190$ nm region of the V_8C_7 nanopowder neutronogram (Fig. 15b) is the reflection of (011) impurity nanocrystalline hexagonal (space group $P\bar{6}m2$) tungsten carbide WC. The admixture of WC appeared as a result of rubbing the milling balls and bowls made from a hard WC – 6 mass % Co alloy.

A quantitative analysis showed that two-phase coarse-crystalline and nanocrystalline vanadium carbide powders contain ~ 21 and ~ 45 mass % of disordered $VC_{0.875}$, respectively. The inset in Fig. 15a presents, as an example, a description of the (222) reflection profile of the V_8C_7 ordered phase and the $(111)_{B1}$ reflection profile of the $VC_{0.875}$ disordered phase. The peak of the disordered phase is roughly three times as wide as that of the ordered phase V_8C_7. Peak broadening in the disordered phase suggests that in the nanopowder obtained by 10 h milling this phase consists of small ($\sim 15-20$ nm) particles in the matrix of the ordered V_8C_7 phase. The microinhomogeneity of V_8C_7 nanoparticles is confirmed by the results of high-resolution transmission electron microscopy (HRTEM). Figure 16 presents an HRTEM image showing inclusions of disordered vanadium carbide $VC_{0.875}$ particles $\sim 8-10$ nm in size within the matrix of the V_8C_7 ordered phase.

Detailed studies of the microstructure of nanocrystalline niobium carbide NbC_y powders ($y = 0.77, 0.84, 0.93, 0.96$) by TOF neutronography are reported in [116, 118, 120–123].

High-resolution neutronographic spectra of all NbC_y samples were obtained at 293 K with the use of a high-resolution HRFD TOF diffractometer operating at channel 5 of the IBR-2 pulsed reactor (JINR, Dubna, Russia). The powders of interest were placed in vanadium containers. The correlation technique ensuring very high resolution power ($\Delta d/d \approx 0.0013$ at $d = 0.2$ nm) was employed for data acquisition and collection. The resolving power $\Delta d/d$ of the diffractometer in the interplane distance range d_{hkl} from ~ 0.05 to ~ 0.5 nm was virtually independent of d_{hkl}, which made it possible to detect microstrains in domains (crystallites) at the $\varepsilon \geqslant 5 \times 10^{-4}$ level and the mean CSR below

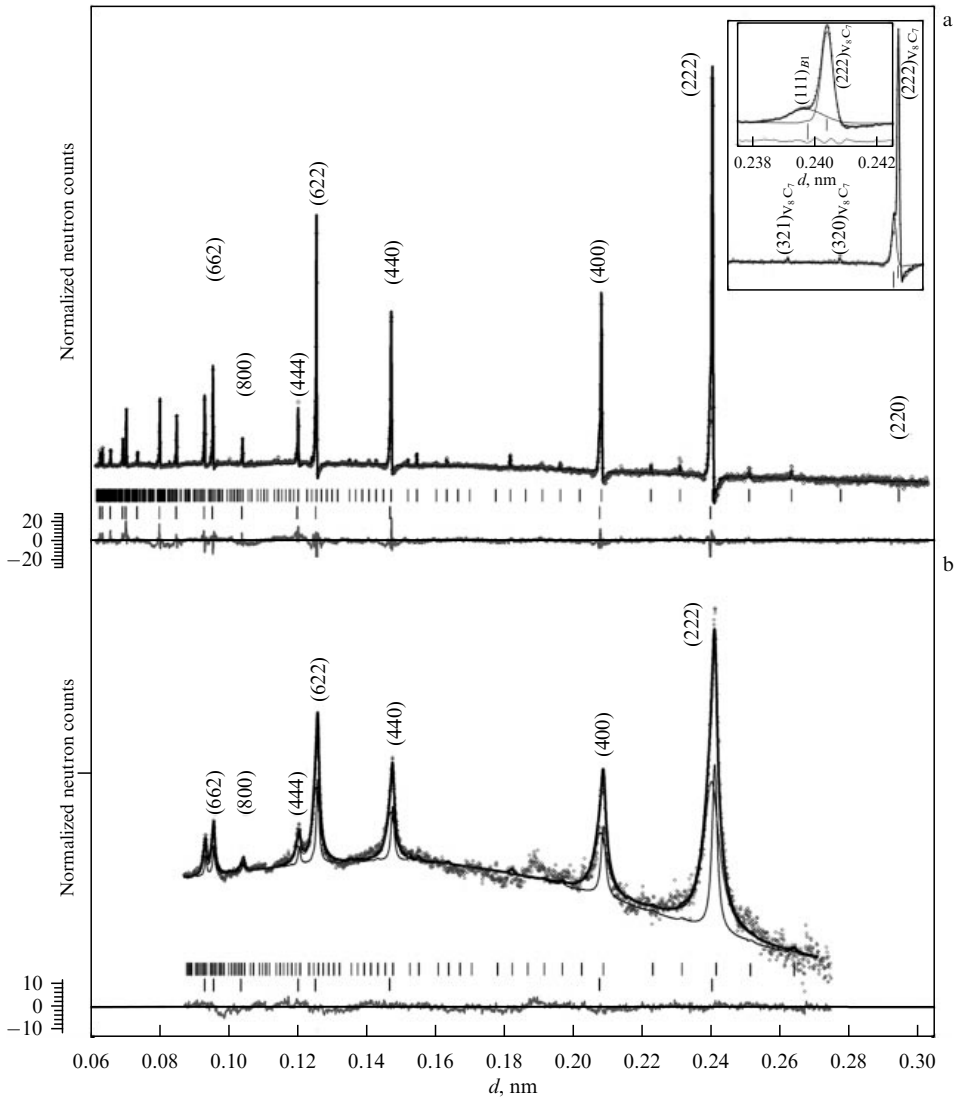

Figure 15. Neutron diffraction patterns of vanadium carbide V_8C_7 [119, 122]: (a) initial coarse-crystalline powder, (b) nanopowder obtained by 10 h of milling. The samples contain a disordered $VC_{0.875}$ phase, besides the ordered V_8C_7 one. Contributions from ordered (narrow peaks) and disordered (broad peaks) phases are shown. The inset presents a description of (222) reflection of the V_8C_7 ordered phase and $(111)_{B1}$ reflection of the $VC_{0.875}$ disordered phase. Vertical bars in top and bottom rows indicate positions of reflections of the ordered V_8C_7 and disordered $VC_{0.875}$ phases, respectively.

350 nm. A reference NIST SRM 676 (Al_2O_3) sample was used to determine the diffractometer resolution function. Analyses of neutronograms by the Rietveld method was performed using FullProf [130] and WPPM [131, 132] software.

X-ray diffraction showed that initial coarse-crystalline niobium carbide powders had a single-phase cubic (space group $Fm\bar{3}m$) $B1$ structure.

The neutron diffraction patterns of initial coarse-crystalline $NbC_{0.77}$, $NbC_{0.84}$, $NbC_{0.93}$, and $NbC_{0.96}6$ and nanopowders obtained from them by ball-milling for 5, 10, and 15 h were measured using an HRFD diffractometer; they are presented in Fig. 17. Diffraction reflections from nanopowders are markedly broadened as a result of milling, and the diffuse background is enhanced. Reflections of the expected ordered monoclinic phase of Nb_6C_5 were not observed in $NbC_{0.84}$ powders. The narrow peaks on neutron diffraction patterns near $d \sim 0.123$, ~ 0.152, and ~ 0.214 nm represent reflections from vanadium containers. Broad peaks on neutron diffraction patterns of NbC_y nanopowders close to $d \sim 0.185-0.190$ nm are (011) reflections of nanocrystalline hexagonal (space group $P\bar{6}m2$) tungsten carbide impurity.

The dependence of the diffraction reflection width Δd on interplanar spacing d is described by function (49).

A quantitative analysis of neutron diffraction data for niobium carbide NbC_y powders revealed that they contain a major nanocrystalline powder fraction together with a small coarse-crystalline one.

Dependences $\beta^2(d^2)$ (Fig. 18) found from HRFD neutron diffraction patterns taking into account the presence of two fractions in NbC_y nanopowders correspond to nanoscale fractions, because the contribution from the coarse-crystalline part is within the measurement error. Dependences $\beta^2(d^2)$ for nanosized phases of all nanopowders are convex curves having different degrees of curvature, which suggests microstrain anisotropy. An approximation of experimental data $\beta^2(d^2)$ for NbC_y nanopowders using dependence (51) taking account of microstrain anisotropy ε_{hkl} enabled the authors of [118, 122, 123] to deduce the ε_{hkl} value and size D of coherent scattering regions.

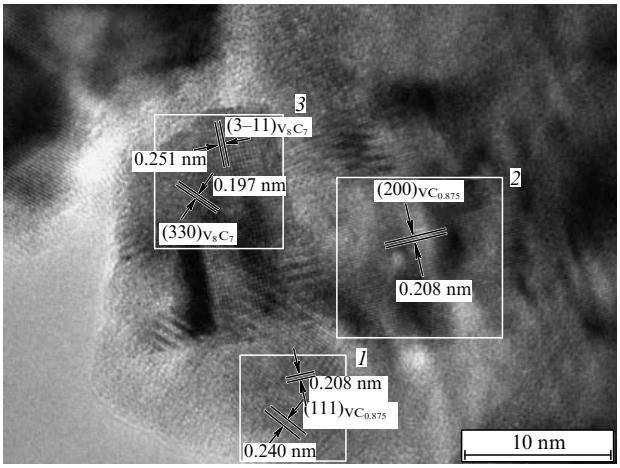

Figure 16. HRTEM images of the microinhomogeneous structure of the V_8C_7 powder obtained by 15 h of milling [119]. The matrix of the ordered V_8C_7 phase contains well apparent inclusions (*1*) and (*2*) of disordered vanadium carbide $VC_{0.875} \sim 8-10$ nm in size. Area (*3*) exhibits only the ordered V_8C_7 phase.

A quantitative analysis of neutron diffraction data indicates that diffraction reflection profiles are most adequately described by taking account of two cubic (space group $Fm\bar{3}m$) fractions in a powder with different lattice constants, compositions, and mean particle sizes. This very important result was obtained for the first time by TOF neutronography. The observed diffraction reflections are the sum of two (wide and narrow) peaks corresponding to nanosized F_1 and coarse-crystalline F_2 fractions, respectively. Figure 19 exemplifies the decomposition of $(200)_{B1}$ diffraction reflections from $NbC_{0.77}$ and $NbC_{0.96}$ powders into peaks corresponding to NbC cubic fractions F_1 and F_2 with different lattice constants, compositions, and mean particle sizes [118, 123, 133]. The main contribution (> 93%) to reflection comes from the broad peak characteristic of the nanoscale F_1 fraction and displaced to the region of smaller d with respect to the narrow peak. The same feature is observed for all reflections on neutron diffraction patterns of NbC_y nanopowders. Thus, niobium carbide nanopowders contain two cubic fractions F_1 and F_2 having different lattice constants and mean particle sizes. The content of the coarse-crystalline nanofraction depends on milling time and decreases from 5–7% to 0 as the duration of milling increases from 1–5 h to 15 h.

Similar data were reported earlier as regards the microinhomogeneous structure of PbS [134, 135] and Ag_2S [136–139] even though their nonstoichiometry is less pronounced than in niobium carbide.

Figure 20 presents calculated anisotropic distributions of ε_{hkl} microstrains along nonequivalent directions $[hkl]$ in $NbC_{0.77}$ and $NbC_{0.96}$ nanopowders produced by ball milling for 10 and 15 h, respectively [118, 123].

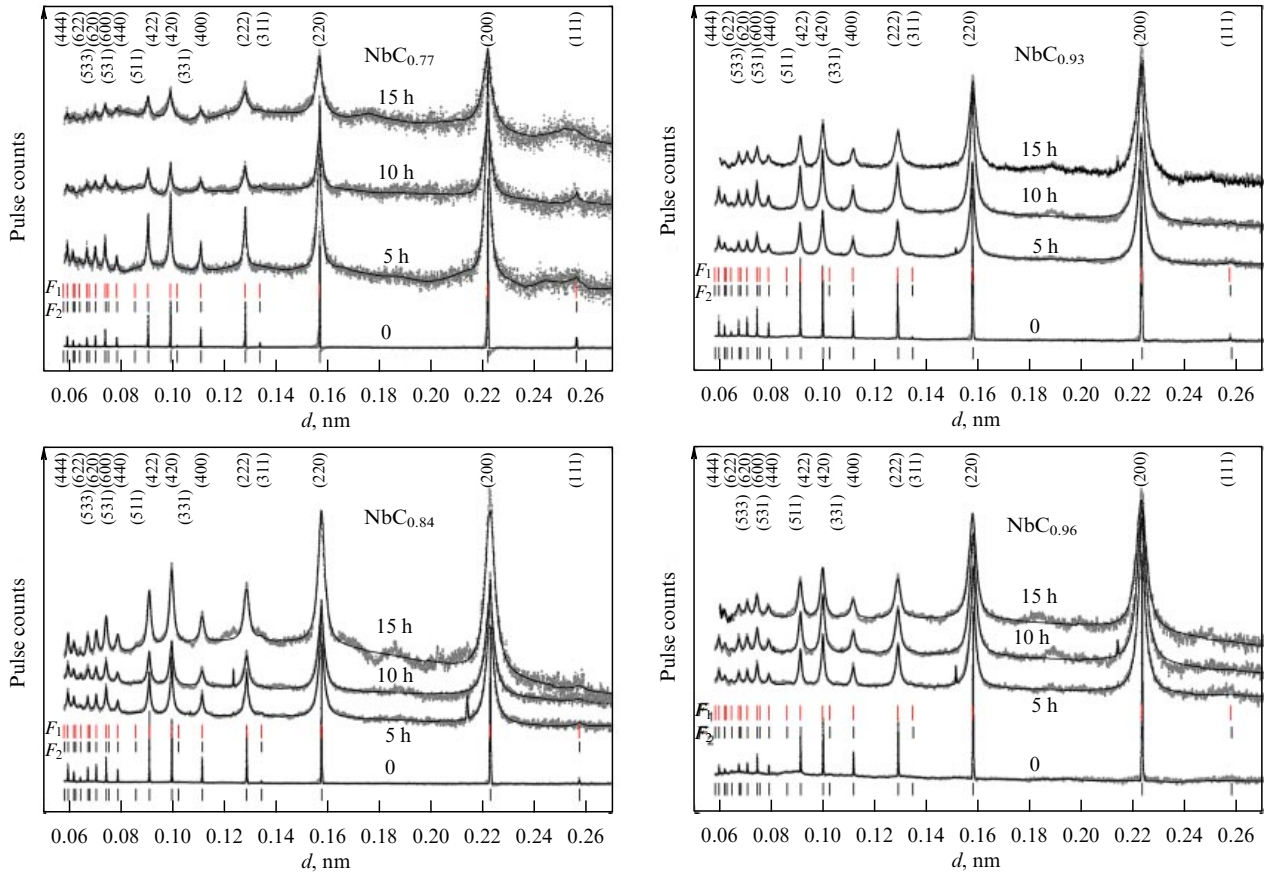

Figure 17. Neutron diffraction patterns of initial coarse-crystalline $NbC_{0.77}$, $NbC_{0.84}$, $NbC_{0.93}$, and $NbC_{0.96}$ powders ($t = 0$) and nanopowders prepared from them by milling for 5, 10, and 15 h [118, 123]. Experimental points and theoretical neutron diffraction patterns are presented. Vertical bars in top and bottom rows indicate calculated positions of reflections of nanoscale F_1 and coarse-crystalline F_2 fractions, respectively. Diffraction reflections of the nanoscale fraction F_1 are shifted to the region of smaller d compared with those of the F_2 fraction. The peaks on neutronograms near ~ 0.123, ~ 0.152, and ~ 0.214 nm are reflections from vanadium containers.

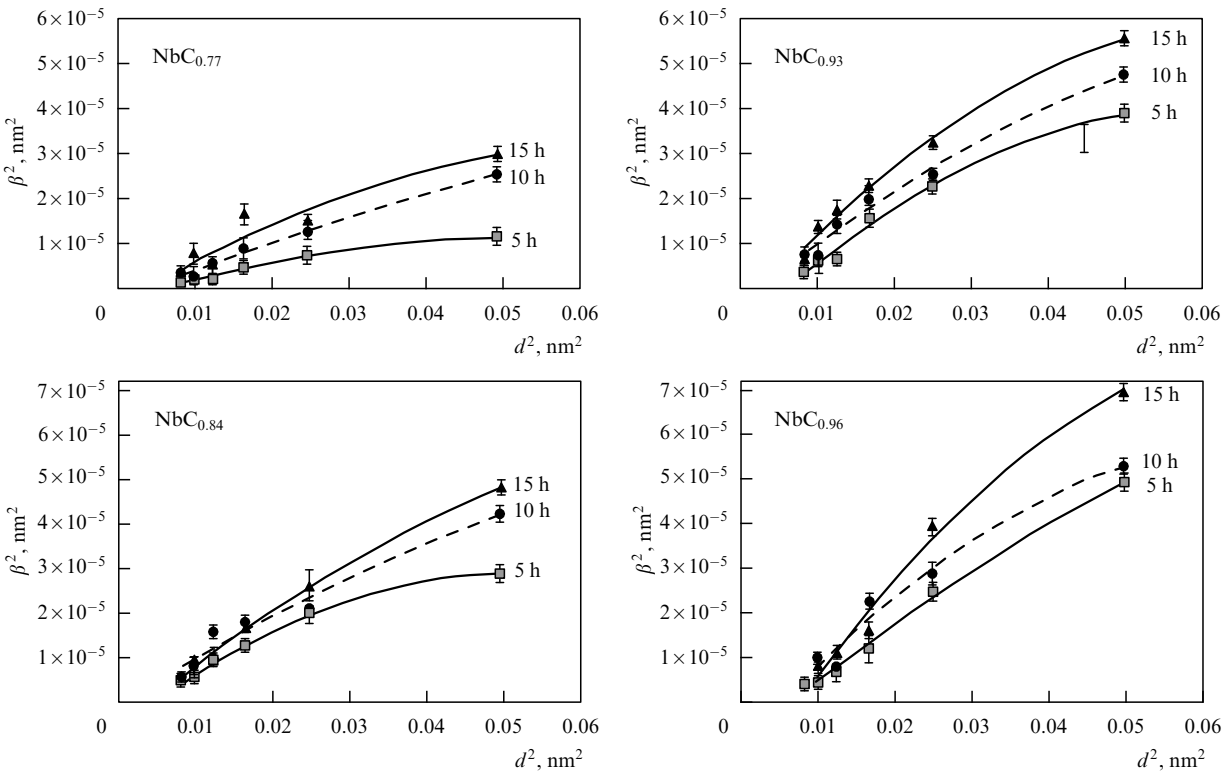

Figure 18. Experimental dependences $\beta^2(d^2)$ of the square of diffraction reflection broadening, β^2, for nanoscale fractions of NbC_y nanopowders ($y = 0.77, 0.84, 0.93, 0.96$) obtained by milling for 5, 10, and 15 h as a function of the square of interplanar spacing d^2 [118, 122, 123]. Reflection width is defined taking account of correction for the diffractometer resolution function.

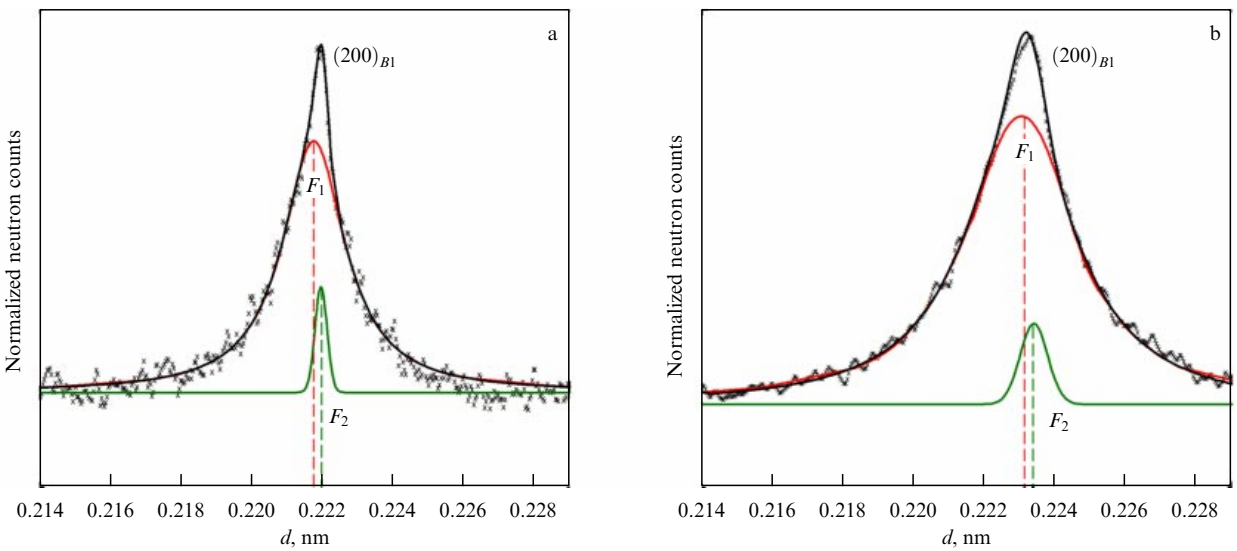

Figure 19. Decomposition of $(200)_{B1}$ diffraction reflections into peaks corresponding to niobium carbide cubic fractions F_1 and F_2 with different lattice constants, compositions, and mean particle sizes [118, 123]: (a) $NbC_{0.77}$ and (b) $NbC_{0.96}$ nanopowders obtained by 5 h of milling. Experimental points and theoretical curves are presented.

5. Application of carbide and oxide nanopowders prepared by ball milling

Strongly nonstoichiometric compounds like carbides and oxides find wide application in modern industry [84, 85]. Their production in the nanocrystalline state with nanometer grains (particles) opens up new prospects for practical use.

Nonstoichiometric carbides MC_y ($y \leqslant 1.0$) are currently in high demand for a variety of purposes, including the production of construction, instrumental, and other materials capable of operating under extreme conditions, such as high temperatures, aggressive media, and heavy workload. Finely dispersed powders of nonstoichiometric carbides are used in the production of nanostructured hard alloys [79] for metal-fabricating industries, mining and boring operations or as dopants for dispersion hardening of high-temperature and thermally resistant steels [140, 141].

Nonstoichiometric vanadium and niobium carbides (VC_y and NbC_y) find application as inhibitors of grain growth in hard alloys and dopants in special steels with enhanced

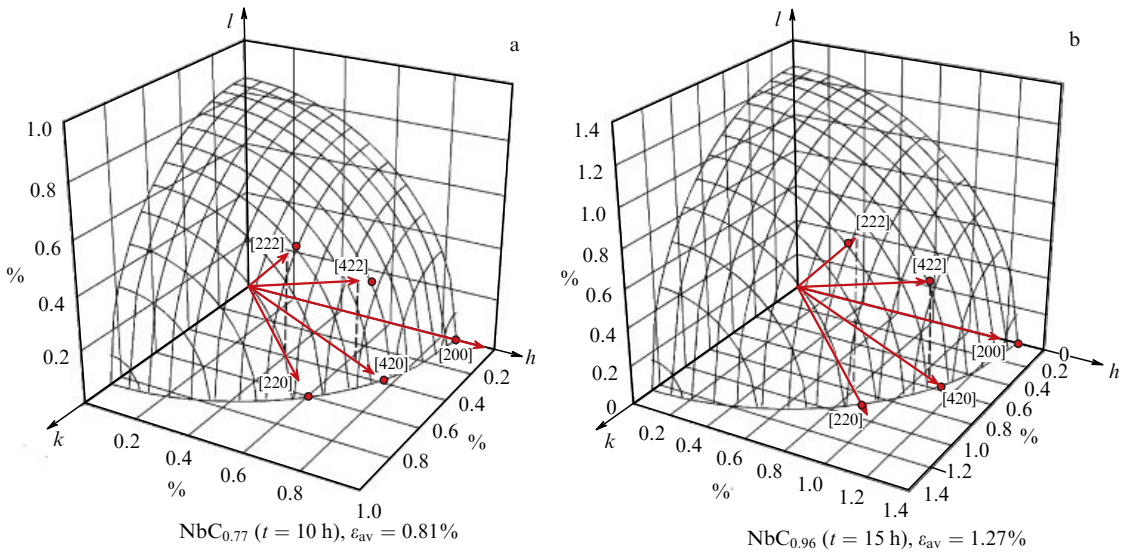

Figure 20. Distribution of microstrains ε_{hkl} in nonequivalent directions $[hkl]$ [118, 123]: (a) $NbC_{0.77}$ nanopowder prepared by 10 h of milling, $\varepsilon_{av} = 0.0081$ (or 0.81%), (b) $NbC_{0.96}$ nanopowder prepared by 15 h of milling, $\varepsilon_{av} = 0.0127$ (or 1.27%). The radii of the spheres are proportional to ε_{av}, and the vector length in $[hkl]$ directions to microstrain ε_{hkl}.

thermal stability and mechanical strength [142]. Cast iron and steel doping with vanadium and niobium carbides is known to cause a release of dispersed nanoscale carbide particles in a metallic matrix in the form of cubic (space group $P4_332$) M_8C_7 or monoclinic (space group $C2/m$) M_6C_5 ordered phases [88, 140, 141].

Titanium oxide-based compounds are used as catalysts for photoelectrochemical water decomposition and photocatalysts for the removal of organic impurities. Titanium dioxide TiO_2 is characterized by a wide band gap (> 3.1 eV); therefore, it absorbs sunlight only in the UV range. To reduce the width of the band gap and obtain a photocatalyst active under sunlight, titanium dioxide is produced in the nanocrystalline state; also, various ions and vacancies are inserted into its sublattices or titanium subdioxides, e.g., cubic titanium monoxide.

An interesting property of titanium and vanadium monoxides is the concentration metal-semiconductor transition: monoxides MO_y with a substoichiometric composition $(y < 1)$ have metallic conductivity, while monoxides with the superstoichiometric composition $(y > 1)$ are actually narrow-gap semiconductors [143]. The metal-semiconductor phase transition is more pronounced in nanocrystalline monoxides. This effect can be used to design new micro- and nanoelectronic devices. Equally deserving of note is the presence of octahedral clusters in different fractions of titanium monoxide [144] and the influence of the small size of its particles on magnetic susceptibility [145, 146].

Niobium monoxide NbO possesses superconductivity properties [147] and is a potentially suitable candidate for manufacturing high-capacity condensers [148].

A variety of chemical methods are currently available for producing nanocrystalline carbides and oxides from suitable precursors. Specifically, carbothermal vacuum reduction of niobium oxide Nb_2O_5 was proposed and implemented to prepare nanocrystalline carbides, e.g., niobium carbide, at ~ 1300 K with the use of melamine $C_3N_3(NH_2)_3$ [149]. Thus far, however, the precursor-based methods allow synthesizing only stoichiometric but not nonstoichiometric nanocrystalline compounds. Therefore, high-energy ball milling of coarse-crystalline compounds preliminarily synthesized by high-temperature sintering remains the principal method for the production of nonstoichiometric nanocrystalline carbides and oxides.

6. Conclusions

High-energy ball milling is a top-down nanotechnology [150] based on the grinding of large particles or grains to nanoscale size.

The main parameter of powder milling in planetary ball mills is the milling energy, proportional to the milling time t and the cube of angular velocity of rotation ω^3, while the size of resulting particles is a function of milling duration t, mass M, and particle size D_{in} of the initial powder. The size of the particles obtained by ball milling depends on the mechanical properties (elastic moduli, Poison coefficient) of the substance being treated. All other conditions being equal, the duration of milling t is the most important parameter. Usually, t is chosen so as to achieve a stable equilibrium between destruction and cold welding of powder particles.

The technological parameters of milling are the ratio of grinding ball mass to powder mass and the use of milling fluids. The standard ratio of grinding ball mass to powder mass is 10:1. The milling fluids include, depending on the composition of the substance to be ground, organic compounds (methanol, ethanol, isobutanol, butanol, hexane, isopropanol, stearic acid, polyethylene glycol, etc.) acting as surface active agents. They are adsorbed on the powder particle surface and reduce to a minimum cold welding of the particles to one another. The amount of the added milling fluids varies from 3 to 30% of the total powder mass.

Materials of different hardness (from soft to extremely hard) are milled in steel grinding bowls with a layer of agate SiO_2, sintered corundum Al_2O_3, silicon nitride Si_3N_4, zirconium oxide ZrO_2, or stabilized yttrium oxide Y_2O_3 lining the inner wall. Superhard materials like carbides are milled in bowls with the inner wall coated with a hard WC–6 wt % alloy with a cobalt binder. In this case, grinding balls from the same alloy are used. To prevent oxidation, all

powders except higher oxides are ground in a vacuum or inert argon atmosphere.

The high-energy ball milling model takes into consideration such properties of the substance chosen for grinding as density, crystalline structure, Burgers vectors, elasticity moduli, Poisson coefficient, and atomization energy, which allows adequately describing the dependence of the particle size not only on given milling parameters but also on the real composition of nonstoichiometric carbides, oxides, nitrides, borides, and ceramic materials based on solid solutions. This is confirmed by the numerous results obtained in experiments on high-energy ball milling of tungsten, vanadium, niobium and tantalum carbides, titanium, vanadium, niobium oxides, and other compounds.

Nanopowders prepared by high-energy ball milling are heavily deformed substances with a microstructure containing very apparent microstrains. The study of such microstructures in ball-milled nanopowders by X-ray and neutron diffraction methods requires taking into account that broadening of diffraction reflections is due to both the small particle size and anisotropic deformation distortions of the crystal lattice. Another feature of ball-milled nanopowders is the inhomogeneous microstructure conditioned by the presence of a small (3–5%) coarse-crystalline fraction, besides the main nanocrystalline one. Prolongation of the milling duration permits reducing to zero the amount of the coarse-crystalline fraction and maintaining the homogeneous microstructure of nanopowders.

Generally speaking, high-energy ball milling allows preparing sufficiently pure carbide and oxide nanopowders with a controllable crystalline structure, microstructure, and mean particle size (20–30 nm). To date, this technology has been the main method for producing nonstoichiometric carbides and oxides in the nanocrystalline state.

Preparing nanopowders with a narrow particle size distribution, i.e., improving the selectivity of the process, remains an unresolved problem. The narrow controlled distribution of nanoparticles by size is a precondition for their application in catalysis and microelectronics and making hard nanostructured alloys. Numerous experiments have demonstrated that the smallest, largest, and intermediate size of nanoparticles in a powder obtained by high-energy ball milling can differ widely (by a factor of 7–10 and even 12–20), depending on the chemical nature of the material in question.

Another problem awaiting solution arises from the enhancement of particle agglomeration with an increase in milling duration. Investigations into the milling of carbides and oxides indicate that the particle size decreases most strikingly at the early milling stages when milling time does not exceed 3–4 h. Its further increase results in a reduction in nanoparticle size and simultaneous agglomeration. It necessitates the optimization of high-energy milling duration and a search for surface active agents used as milling fluids and most effectively preventing nanoparticle agglomeration. Optimization of the duration of milling with a view to its shortening and termination upon achieving the desired size of nanoparticles will contribute, inter alia, to a reduction in nanopowder contamination by the material of milling balls and bowls.

This study was supported by the Russian Science Foundation (grant No. 19-73-20012) through the Institute of Solid-State Chemistry of the Ural Branch of the RAS.

References

1. Gusev A I *Phys. Usp.* **41** 49 (1998); *Usp. Fiz. Nauk* **168** 55 (1998)
2. Gusev A I, Rempel À À *Nanokristallicheskie Materialy* (Nanocrystalline Materials) 2nd ed. (Moscow: Fizmatlit, 2001)
3. Gusev A I, Rempel A A *Nanocrysnalline Materials* (Cambridge: Cambridge Intern. Sci. Publ., 2004)
4. Gusev A I, in *Dekker Encyclopedia of Nanoscience and Nanotechnology* Vol. 3 (Eds J A Schwarz, C Contescu, K Putyera) (New York: M. Dekker, 2004) p. 2289
5. Gusev A I *Nanomaterialy, Nanostruktury, Nanotekhnologii* (Nanomaterials, Nanostructures, Nanotechnologies) 3rd ed. (Moscow: Fizmatlit, 2009)
6. Avvakumov E G *Mekhanicheskie Metody Aktivatsii Khimicheskikh Protsessov* (Mechanical Methods for Activation of Chemical Processes) (Novosibirsk: Nauka, 1989)
7. Butyagin P Yu *Russ. Chem. Rev.* **63** 965 (1994); *Usp. Khim.* **63** 1031 (1994)
8. Balogh J et al. *Nanostruct. Mater.* **2** 11 (1993)
9. Teresiak A, Kubsch H *Nanostruct. Mater.* **6** 671 (1995)
10. Xueming M A, Gang J I *J. Alloys Comp.* **245** L30 (1996)
11. Yavuz M et al. *Supercond. Sci. Technol.* **11** 1153 (1998)
12. Coste S et al. *J. Alloys Comp.* **434–435** 489 (2007)
13. Venugopal T, Rao K P, Murty B S *J. Nanosci. Nanotechnol.* **7** 2376 (2007)
14. Wang Y et al. *Nanotechnology* **18** 465701 (2007)
15. Suryanarayana C *Prog. Mater. Sci.* **46** 1 (2001)
16. Baláž P *Mechanochemistry in Nanoscience and Minerals Engineering* (Berlin: Springer, 2008)
17. Alves A P, Bergmann C P, Berutti F A *Novel Synthesis and Chatracterization of Nanostructured Materials* (Berlin: Springer, 2013)
18. Kuriki Y et al. *Fuel Proc. Technol.* **59** 189 (1999)
19. Han S-C et al. *J. Alloys Comp.* **351** 273 (2003)
20. Estrada-Guel I et al. *Microsc. Microan.* **22** 1630 (2016)
21. Sharma P, Sharma S, Khanduja D *Mater. Manufact. Proc.* **30** 1370 (2015)
22. Boldyrev V V, in *Mekhanicheskie Metody Aktivatsii Khimicheskikh Protsessov* (Mechanical Methods for Activation of Chemical Processes) (Ed. E G Avvakumov) (Novosibirsk: Nauka, 1988) p. 5
23. Zhurkov S N, Narzulaev B N *Zh. Tekh. Fiz.* **23** 1677 (1953)
24. Regel' V R, Slutsker A I, Tomashevskii É E *Sov. Phys. Usp.* **15** 45 (1972); *Usp. Fiz. Nauk* **106** 193 (1972)
25. Butyagin P Yu, in *Advances in Mechanochemistry*: *Physical and Chemical Processes under Deformation* (Chemistry Reviews, Vol. 23, Eds P Butyagin, A Dubinskaya) (Chur: Harward Acad. Publ., 1998) p. 91
26. Putra I S, Suharto D (Eds) *Fracture and Strength of Solids VI, Proc. of the 6th Intern. Conf. on Fracture and Strength of Solids, FEOFS 2005, April 4 – 6, 2005, Bali, Indonesia* (Key Engineering Materials, Vol. 306–308) (Enfield, NH: Trans Tech Publ., 2006)
27. Sieradzki K *J. Phys. C* **18** L855 (1985)
28. Butyagin P Yu, in *Mekhanicheskie Metody Aktivatsii Khimicheskikh Protsessov* (Mechanical Methods for Activation of Chemical Processes) (Ed. E G Avvakumov) (Novosibirsk: Nauka, 1988) p. 32
29. Fecht H-J *Nanostruct. Mater.* **6** 33 (1995)
30. Mohamed F A *Acta Mater.* **51** 4107 (2003)
31. Boiko V F, Verkhoturov A D *Perspekt. Mater.* (6) 84 (2008)
32. Eckert J et al. *J. Mater. Res.* **7** 1751 (1992)
33. Oleszak D, Shingu P H *J. Appl. Phys.* **79** 2975 (1996)
34. Kurlov A S, Gusev A I *Tech. Phys. Lett.* **33** 828 (2007); *Pis'ma Zh. Tekh. Fiz.* **33** (19) 46 (2007)
35. Gusev A I, Kurlov A S *Nanotechnology* **19** 265302 (2008)
36. Gusev A I, Kurlov A S *Inorg. Mater.* **45** 35 (2009); *Neorg. Mater.* **45** 38 (2009)
37. Kurlov A S, Gusev A I, in *17 Plansee Seminar 2009*: *Proc. Intern. Conf. on High Performance P/M Materials, Reutte, Austria, May 25 – 29, 2009* (Eds L S Sigl, P Rödhammer, H Wildner) Vol. 3 (Reutte, Austria: Plansee Group, 2009) p. GT24/1
38. Kurlov A S, Gusev A I, in *Mathematical Modeling and Computer Simulation of Material Technologies, Proc. 6th Intern. Conf. MMT-2010, Ariel, Israel, August 23–27, 2010* (Ed. M Zinigrad) (Ariel, Israel: Ariel Univ. Center of Samaria, 2010) p. 1-105

39. Kurlov A S, Gusev A I *Tech. Phys.* **56** 975 (2011); *Zh. Tekh. Fiz.* **81** (7) 76 (2011)
40. Neiman G W, Weertman J R, Siegel R W *J. Mater. Res.* **6** 1012 (1991)
41. Jang J S C, Koch C C *Scripta Metall. Mater.* **24** 1599 (1990)
42. Fougere G E, Weertman J R, Siegel R W *Nanostruct. Mater.* **3** 379 (1993)
43. Siegel R W, Fougere G E *Nanostruct. Mater.* **6** 205 (1995)
44. Ishida Y et al. *Nanostruct. Mater.* **6** 115 (1995)
45. Inoue A, Shibata T, Masumoto T *Mater. Trans. Jpn. Inst. Met.* **33** 491 (1992)
46. Tairov Yu M, Tsvetkov V F *J. Cryst. Growth* **52** 146 (1981)
47. Wang X, Cai D, Zhang H *J. Cryst. Growth* **305** 122 (2007)
48. Panov V S *Izv. Vyssh. Uchebn. Zaved. Ser. Tsvetn. Metallurg.* (2) 63 (2007)
49. Kurlov A S, Rempel A A *Inorg. Mater.* **45** 380 (2009); *Neorg. Mater.* **45** 428 (2009)
50. Berger S, Porat R, Rosen R *Prog. Mater. Sci.* **42** 311 (1997)
51. Kurlov A S et al. *Dokl. Chem.* **439** 213 (2011); *Dokl. Ross. Akad. Nauk* **439** 215 (2011)
52. Trampenau J et al. *Nanostruct. Mater.* **6** 551 (1995)
53. Novotny V, Meincke P P M, Watson J H P *Phys. Rev. Lett.* **28** 901 (1972)
54. Goll G, Löhneyen H *Nanostruct. Mater.* **6** 559 (1995)
55. Sadovnikov S I, Gusev A I *J. Alloys Comp.* **610** 196 (2014)
56. Sadovnikov S I, Gusev A I *Phys. Solid State* **56** 2353 (2014); *Fiz. Tverd. Tela* **56** 2274 (2014)
57. Sadovnikov S I, Gusev A I, Rempel A A *Russ. Chem. Rev.* **85** 731 (2016); *Usp. Khim.* **85** 731 (2016)
58. Sadovnikov S I, Rempel A A, Gusev A I *Nanostructured Lead, Cadmium and Silver Sulfides*: *Structure, Nonstoichiometry and Properties* (Cham: Springer Intern. Publ. AG, 2018)
59. Sadovnikov S I, Gusev A I, Rempel A A *Poluprovodnikovye Nanostruktury Sul'fidov Svintsa, Kadmiya i Serebra* (Semiconductor Nanostructures of Lead, Cadmium, and Silver Sulfides) (Moscow: Fizmatlit, 2018)
60. Gusev A I et al. *Phys. Solid State* **58** 251 (2016); *Fiz. Tverd. Tela* **58** 246 (2016)
61. Sadovnikov S I et al. *Phys. Chem. Chem. Phys.* **18** 4617 (2016)
62. Sadovnikov S I, Gusev A I *Phys. Solid State* **59** 1887 (2017); *Fiz. Tverd. Tela* **59** 1863 (2017)
63. Sadovnikov S I, Gusev A I *J. Mater. Chem. A* **5** 17676 (2017)
64. Sadovnikov S I, Gusev A I *J. Therm. Anal. Calor.* **131** 1155 (2018)
65. Gusev A I, Sadovnikov S I *Thermochim. Acta* **660** 1 (2018)
66. Sadovnikov S I, Rempel A A, Gusev A I *Russ. Chem. Rev.* **87** 303 (2018); *Usp. Khim.* **87** 303 (2018)
67. Fang X et al. *Prog. Mater. Sci.* **56** 175 (2011)
68. Sadovnikov S I *Russ. Chem. Rev.* **88** 571 (2019); *Usp. Khim.* **88** 571 (2019)
69. Butyagin P Yu, Streletskii A N *Phys. Solid State* **47** 856 (2005); *Fiz. Tverd. Tela* **47** 830 (2005)
70. Nazarov A A, Romanov A E, Valiev R Z *Nanostruct. Mater.* **4** 93 (1994)
71. Williamson G K, Smallman R E *Phil. Mag. 8* **1** 34 (1956)
72. Kurlov A S, Gusev A I *Int. J. Refr. Met. Hard Mater.* **46** 125 (2014)
73. Kosolapova T Ya (Ed.) *Handbook of High Temperature Compounds*: *Properties, Production, Applications* (New York: Hemisphere, 1990); Translated from Russian: *Svoistva, Poluchenie i Primenenie Tugoplavkikh Soedinenii*. Spravochnik (Moscow: Metallurgiya, 1986)
74. Gubicza J et al. *Mater. Sci. Eng. A* **309–310** 60 (2001)
75. Bolton J D, Redington M *J. Mater. Sci.* **15** 3150 (1980)
76. Wicks C E, Block F E *Thermodynamic Properties of 65 Elements*: *Their Oxides, Halides, Carbides and Nitrides* (Washington, DC: U.S. Govt. Print. Off., 1963); Translated into Russian: *Termodinamicheskie Svoistva 65 Elementov, Ikh Okislov, Galogenidov, Karbidov i Nitridov* (Moscow: Metallurgiya, 1965)
77. Glushko V P (Ed.) *Thermodynamic and Thermophysical Properties of Combustion Products* (Jerusalem: Israel Program for Scientific Translations, 1974); Translated from Russian: *Termodinamicheskie Svoistva Individual'nykh Veshchestv* Vols 1–4 (Moscow: Nauka, 1979)
78. Barin I *Thermochemical Data of Pure Substance* 3rd ed. (Weinheim: VCH, 1995)
79. Kurlov A S, Gusev A I *Tungsten Carbides*: *Structure, Properties and Application in Hardmetals* (Cham: Springer, 2013)
80. Williamson G K, Hall W H *Acta Metallurg.* **1** 22 (1953)
81. Hall W H *Proc. Phys. Soc. London A* **62** 741 (1949)
82. Warren B E *X-Ray Diffraction* (New York: Dower Publ., 1990)
83. Gusev A I, Rempel A A *Nestekhiometriya, Besporyadok i Poryadok v Tverdom Tele* (Nonstoichiometry, Disorder and Order in a Solid) (Ekaterinburg: UrO RAN, 2001)
84. Gusev A I, Rempel A A, Magerl A J *Disorder and Order in Strongly Nonstoichiometric Compounds*: *Transition Metal Carbides, Nitrides and Oxides* (Berlin: Springer-Verlag, 2001)
85. Gusev A I *Nestekhiometriya, Besporyadok, Blizhnii i Dal'nii Poryadok v Tverdom Tele* (Nonstoichiometry, Disorder, Long- and Short-Range Order in a Solid) (Moscow: Fizmatlit, 2007)
86. Rempel A A, Gusev A I *Nestekhiometriya v Tverdom Tele* (Nonstoichiometry in a Solid) (Moscow: Fizmatlit, 2018)
87. Kurlov A S, Gusev A I *Phys. Solid State* **55** 2522 (2013); *Fiz. Tverd. Tela* **55** 2398 (2013)
88. Kurlov A S, Gusev A I *J. Alloys Comp.* **582** 108 (2014)
89. Kurlov A S, Bel'kov A M, Vyrodova T D, Gusev A I *Phys. Solid State* **57** 70 (2015); *Fiz. Tverd. Tela* **57** 66 (2015)
90. Kurlov A S, Gusev A I *Inorg. Mater.* **51** 29 (2015); *Neorg. Mater.* **51** 34 (2015)
91. Gusev A I et al. *Phys. Solid State* **57** 1170 (2015); *Fiz. Tverd. Tela* **57** 1149 (2015)
92. Gusev A I et al. *Int. J. Refr. Met. Hard Mater.* **51** 70 (2015)
93. Valeeva A A, Schroettner H, Rempel A A *Inorg. Mater.* **47** 408 (2011); *Neorg. Mater.* **47** 464 (2011)
94. Kurlov A S, Gusev A I *Phys. Solid State* **55** 430 (2013); *Fiz. Tverd. Tela* **55** 385 (2013)
95. Williams W S, Shaal R D *J. Appl. Phys.* **33** 955 (1962)
96. Rowcliffe D J, Hollox G E *Mater. Sci.* **6** 1270 (1971)
97. Hannink R H J, Kohlstedt D L, Murray M J *Proc. R. Soc. London A* **326** 409 (1972)
98. Kurlov A S, Gusev A I *Inorg. Mater.* **49** 347 (2013); *Neorg. Mater.* **49** 359 (2013)
99. Zueva L V, Gusev A I *Russ. J. Phys. Chem.* **73** 690 (1999); *Zh. Fiz. Khim.* **73** 792 (1999)
100. Glushko V P (Ed.) *Termodinamicheskie Svoistva Individual'nykh Veshchestv*. Spravochnik (Thermodynamic Properties of Individual Substances. Reference Book) Vol. 2, Book 1 (Moscow: Nauka, 1979) p. 11; Glushko V P (Ed.) *Termodinamicheskie Svoistva Individual'nykh Veshchestv*. Spravochnik (Thermodynamic Properties of Individual Substances. Reference Book) Vol. 2, Book 1 (Moscow: Nauka, 1979) p. 438
101. Glushko V P (Ed.) *Termodinamicheskie Svoistva Individual'nykh Veshchestv*. Spravochnik (Thermodynamic Properties of Individual Substances. Reference Book) Vol. 4, Book 1 (Moscow: Nauka, 1982) p. 622
102. Toth L *Transition Metal Carbides and Nitrides* (New York: Academic Press, 1971)
103. Williams W S *J. Appl. Phys.* **35** 1329 (1964)
104. Bauccio M (Ed.) *ASM Engineered Materials Reference Book* 2nd ed. (Materials Park, OH: ASM Intern., 1994)
105. Valeeva A A et al. *Tech. Phys.* **54** 1618 (2009); *Zh. Tekh. Fiz.* **79** (11) 56 (2009)
106. Valeeva A A, Rempel A A *Perspekt. Mater.* (12) 71 (2011)
107. Valeeva A A, Schrottner H, Rempel A A *Russ. Chem. Bull.* **63** 2729 (2014); *Izv. Ross. Akad. Nauk Ser. Khim.* **12** 2729 (2014)
108. Valeeva A A et al. *Inorg. Mater.* **51** 1132 (2015); *Neorg. Mater.* **51** 1221 (2015)
109. Valeeva A A, Schroettner H, Rempel A A *Inorg. Mater.* **50** 398 (2014); *Neorg. Mater.* **50** 430 (2014)
110. Taylor A, Doyle N J, in *The Chemistry of Extended Defects in Non-Metallic Solids* (Eds L Eyring, M O'Keeffe) (Amsterdam: North-Holland, 1970) p. 523
111. Scherrer P *Nachr. Ges. Wiss. Göttingen Math. Phys. Kl.* **2** 98 (1918)
112. Seljkow N *Z. Phys.* **31** 439 (1925)
113. Krivoglaz M A *Theory of X-ray and Thermal-Neutron Scattering by Real Crystals* (New York: Plenum Press, 1969); Translated from

Russian: *Teoriya Rasseyaniya Rentgenovskikh Luchei i Teplovykh Neitronov Real'nymi Kristallami* (Moscow: Nauka, 1967)
114. Stokes A R, Wilson A J C *Proc. Phys. Soc. London* **56** 174 (1944)
115. Scardi P, Ortolani M, Leoni M *Mater. Sci. Forum* **651** 155 (2010)
116. Kurlov A S, Bobrikov I A, Balagurov A M, Gusev A I *JETP Lett.* **100** 629 (2014); *Pis'ma Zh. Eksp. Teor. Fiz.* **100** 712 (2014)
117. Gusev A I et al. *JETP Lett.* **102** 154 (2015); *Pis'ma Zh. Eksp. Teor. Fiz.* **102** 179 (2015)
118. Balagurov A M et al. *Mater. Characterizat.* **109** 173 (2015)
119. Kurlov A S et al. *Superlatt. Microstruct.* **90** 148 (2016)
120. Kurlov A S et al. *Phys. Solid State* **59** 607 (2017); *Fiz. Tverd. Tela* **59** 588 (2017)
121. Kurlov A S et al. *Cryst. Res. Technol.* **52** 1700061 (2017)
122. Kurlov A S et al. *JETP Lett.* **108** 154 (2018); *Pis'ma Zh. Eksp. Teor. Fiz.* **108** 253 (2018)
123. Kurlov A S et al. *Asian Res. J. Curr. Sci.* **1** ARJOCS.61 (2018)
124. Mittemeijer E J, Welzel U *Z. Kristallogr.* **223** 552 (2008)
125. Leoni M, Martinez-Garcia J, Scardi P *J. Appl. Crystallogr.* **40** 719 (2007)
126. Dragomir I C, Ungár T *Powder Diffract.* **17** 104 (2002)
127. Lucks I, Lamparter P, Mittemeijer E J *J. Appl. Cryst.* **37** 300 (2004)
128. Ungár T *Powder Diffract.* **23** 125 (2008)
129. Balagurov A M *Neutron News* **16** 8 (2005)
130. Rodríguez-Carvajal J *Physica B* **192** 55 (1993)
131. Scardi P, Leoni M *Acta Cryst. A* **58** 190 (2002)
132. Leoni M, Scardi P *J. Appl. Crystallogr.* **37** 629 (2004)
133. Gusev A I *Solid State Sci.* **100** 106092 (2020)
134. Sadovnikov S I et al. *Inorg. Mater.* **48** 21 (2012); *Neorg. Mater.* **48** 26 (2012)
135. Sadovnikov S I, Rempel A A *Dokl. Phys. Chem.* **428** 167 (2009); *Dokl. Ross. Akad. Nauk* **428** 48 (2009)
136. Sadovnikov S I, Rempel A A *Inorg. Mater.* **51** 759 (2015); Neorg. Mater. **51** 829 (2015)
137. Sadovnikov S I, Gusev A I, Rempel A A *Rev. Adv. Mater. Sci.* **41** 7 (2015)
138. Sadovnikov S I, Chukin A V, Rempel A A, Gusev A I *Phys. Solid State* **58** 30 (2016); *Fiz. Tverd. Tela* **58** 32 (2016)
139. Sadovnikov S I et al. *Int. J. Hydrogen Energy* **42** 25258 (2017)
140. Dunlop G L, Porter D A *Scand. J. Metall.* **6** 19 (1977)
141. Kesri R, Hamar-Thibault S *Acta Metall.* **36** 149 (1988)
142. Huang S G et al. *Int. J. Refr. Met. Hard Mater.* **26** 389 (2008)
143. Valeeva A A, Rempel A A, Gusev A I *JETP Lett.* **73** 621 (2001); *Pis'ma Zh. Eksp. Teor. Fiz.* **73** 702 (2001)
144. Kostenko M G, Valeeva A A, Rempel A A *Mendeleev Commun.* **22** 245 (2012)
145. Valeeva A A, Nazarova S Z, Rempel A A *JETP Lett.* **101** 258 (2015); *Pis'ma Zh. Eksp. Teor. Fiz.* **101** 276 (2015)
146. Valeeva A A, Nazarova S Z, Rempel A A *Phys. Solid State* **58** 772 (2016); *Fiz. Tverd. Tela* **58** 747 (2016)
147. Hulm J K et al. *J. Low Temp. Phys.* **7** 291 (1972)
148. Motchenbacher C A et al., Patent No. US 7157073 B2 (2007)
149. Lei M et al. *J. Eur. Ceramic Soc.* **28** 1671 (2008)
150. Rempel A A *Russ. Chem. Rev.* **76** 435 (2007); *Usp. Khim.* **76** 474 (2007)